S960 STEEL GRADE SQUARE BIRD-BEAK T- AND X-JOINTS: NUMERICAL INVESTIGATION AND DESIGN

Madhup Pandey[1,*] and Ben Young[2]

[1]*Department of Civil Engineering, University of Nottingham, Nottingham, United Kingdom.*
[2]*Department of Civil and Environmental Engineering, The Hong Kong Polytechnic University, Hong Kong, China.*

Abstract

The detailed numerical investigation and design of cold-formed S960 steel grade square bird-beak (SBB) T- and X-joints have been presented in this paper. The SBB joint is one of the novel bird-beak tubular joint configurations and obtained by rotating the chord member of a conventional square hollow section (SHS) joint along its centroidal axis by 45°. In this investigation, accurate finite element (FE) models were developed for SBB T- and X-joints using the tests carried out by the authors. The developed FE models successfully replicated the static strengths, load vs deformation curves and failure modes of test specimens. In order to gain an in-depth understanding on the static behaviour of SBB joints, a comprehensive FE parametric study was performed using the verified FE models. The joint failure strengths and joint ultimate capacities of a total of 220 SBB T- and X-joints specimens, including 200 FE specimens investigated in this study, were evaluated against the nominal strengths predicted from the literature and European code. All SBB T- and X-joints test and FE specimens were failed by the chord crown failure (C) mode. It has been shown that the design provisions given in the literature and European code are unsuitable and uneconomical for the design of cold-formed S960 steel grade SBB T- and X-joints investigated in this study. Therefore, accurate and reliable design equations are proposed in this study for predicting the static strengths of the investigated SBB T- and X-joints.

Keywords: Cold-formed steel; Design rules; FE analysis; High strength steel; Square bird-beak joints; S960 steel; Tubular joints.

---

*Corresponding author. (e-mail: madhup.pandey@nottingham.ac.uk).

1. Introduction

Tubular members are widely used as the primary load carrying elements in many structures subjected to different types of loading, including topsides and jackets of offshore structures, agricultural equipment, booms and jibs of cranes, wheels, bridges, towers, trusses, spatial structures, stadiums, buildings, prefabricated modular structures and so on. In the last six decades, numerous analytical, experimental and numerical investigations were carried out on different types of conventional tubular joints that were subjected to static and fatigue loads. In this study, conventional tubular joints are referred to those joints where braces and chords are not rotated about their corresponding centroidal axes. The findings of the investigations carried out on normal strength steel (in this study, referred to steels with steel grades lower than or equal to S460) conventional tubular joints formed the basis of the existing design rules. By applying material factor (C_f) on design rules developed for S355 or lower steel grades tubular joints, the proposed design rules are now extended up to S700 steel grade. Apart from conventional tubular joints, bird-beak joints represent one of the new configurations of hollow section joints.

In the bird-beak joints, braces and/or chords are rotated about their respective centroidal axes. Square bird-beak (SBB) is that configuration where only the chord is rotated about its centroidal axis. In addition to the aesthetic superiority of SBB configuration, it also brings many other technical advantages, including (a) smooth transfer of load from brace to chord members, which averted the development of bending and buckling in the chord member; (b) high stiffness around the brace-chord junction; (c) less hindrance for wind loads; and (d) enhanced ultimate capacities of joints. The practical applications of bird-beak joints can be seen in the convention centre in Minneapolis (Minnesota, USA), national stadium (Beijing, China) and Takishita bridge (Ibaraki, Japan). High strength steel (HSS) (in this study, referred to steels with steel grades higher than S460) circular, square and rectangular hollow sections (CHS, SHS and RHS) members are in high demand in various civil engineering projects because of their superior strength per unit weight, reduced handling cost and reduced erection time. However, the lack of adequate research work and design recommendations are the primary reasons hampering the widespread use of HSS tubular members. However, some studies have recently been conducted by the authors to investigate the static behaviour of cold-formed high strength steel (CFHSS) member-rotated and conventional tubular T- and X-joints [1-7].

Ono et al. [8] firstly introduced the bird-beak joint configuration by investigating the static strengths of diamond bird-beak (DBB) K- and T-joints. The semi-empirical design equations were subsequently proposed using the test results to predict the ultimate capacities of normal strength steel DBB K- and T-joints. Numerical and analytical methods were used by Davies et al. [9] and Davies and Kelly [10] to determine the static strengths of S275 steel grade DBB K-, X- and T-joints made of SHS (hereafter, RHS also represents SHS) members. A comparative numerical investigation between conventional and DBB X-joints made of S275 steel grade was carried out by Owen et al. [11]. The numerical results obtained after assuming an elasto-plastic material behaviour were used to propose a semi-empirical design equation to predict the static ultimate capacities of the investigated joints. Chen and Wang [12,13] carried out experimental and numerical investigations on Q235 steel grade SBB T-joints and proposed a design equation to predict the ultimate capacities of the investigated joints. Peña and Chacón [14] numerically investigated the static behaviour of DBB X-joints subjected to compression and tensile loads. A detailed parametric study was performed, including steel grades ranging from S235 to S460. The numerical results were used to propose design equations for predicting the compression and tensile ultimate capacities of the investigated joints. Tong et al. [15] studied the fatigue behaviour of cold-formed S235 steel grade DBB T-joints. Based on the fatigue data and stress concentration factors, new fatigue design curves were proposed using the hot spot stress method. It was indicated that DBB T-joints have better fatigue behaviour when the value of β is not greater than 0.7.

The literature review confirms that, except for the experimental investigations carried out by Pandey and Young [1,2], no other research is available on HSS SBB T- and X-joints. Therefore, a comprehensive numerical investigation was performed in this paper using the test results obtained from Pandey and Young [1,2]. It has been demonstrated that the design equation proposed by Chen and Wang [13] is unsuitable for the investigated SBB T- and X-joints. As a result, using two design approaches, accurate, less dispersed and reliable design equations are proposed to predict the joint failure strengths (N_f) and ultimate capacities (N_{max}) of cold-formed S960 steel grade SBB T- and X-joints. In this study, the joint failure strength (N_f) has been defined as the load corresponding to the lower indentation of the chord associated with either ultimate capacity (i.e. peak load) or 3% ultimate deformation limit load. On the other hand, the ultimate capacity (N_{max}) is the load corresponding to the first peak appeared in the load vs chord crown indentation curves.

2. Summary of test programs

Pandey and Young [1,2] carried out test programs to determine the N_f and N_{max} of cold-formed S960 steel grade SBB T- and X-joints. Axial compression loads were applied on the SBB T- and X-joints test specimens through brace members. The chord ends of SBB T-joint test specimens were supported on rollers through specially fabricated V-shaped end blocks. On the other hand, for SBB X-joint test specimens, top brace end was fixed, and vertical displacement was allowed at the bottom brace end. The braces and chords were made of S960 steel grade RHS members. The thermo-mechanically controlled processed plates of S960 steel grade were cold-formed to obtain hollow section members. A fully robotic metal active gas welding was employed to weld braces and chords. In total, 20 tests were conducted, including 10 SBB T-joints and 10 SBB X-joints. Fig. 1 presents various notations for SBB X-joint, which are also valid for SBB T-joint. The static behaviour of these joints primarily depend on non-dimensional geometric ratios, including β' (b_1/b_0'), 2γ (b_0/t_0) and τ (t_1/t_0). The symbols b, h, t and R stand for cross-section width, depth, thickness and external corner radius of RHS member, respectively. The subscripts 0 and 1 denote chord and brace, respectively.

The member-rotation angle about the centroidal axis of chord member was represented by ω. In the test programs, β' varied from 0.25 to 0.62, 2γ varied from 25.3 to 39.1 and τ varied from 0.67 to 1.28. The lengths of braces (L_1) of SBB T- and X-joints were determined as 2×maximum [b_1,h_1] mm. On the other hand, the lengths of chords (L_0) of SBB T- and X-joints were determined as $h_1+3h_0'+180$ mm and h_1+4h_0' mm, respectively. The symbols b_0' and h_0' represent the effective width and depth of chord cross-section, respectively, and are equal to $\sqrt{b_0^2+h_0^2}-0.83R_0$. The measured static 0.2% proof stresses of RHS members varied from 952 to 1059 MPa, while the measured static

0.2% proof stress of welding filler material was 965 MPa. All SBB T- and X-joint test specimens were failed by chord crown failure (C) mode. In addition, for all test specimens, the N_f was controlled by the 3% ultimate deformation limit load, which was taken as the load corresponding to the 0.03 $b_0^{'}$ indentation in the load vs chord crown indentation curves. The term $b_0^{'}$ is the effective width of the rotated chord member and equal to $\sqrt{b_0^2 + h_0^2} - 0.83R_0$. The test results were obtained in the form of N vs u curves, where N and u respectively stand for static load and indentation at the crown location of the chord member. The testing machine was paused for 120 seconds at two different locations in each test. The load drops captured during the pauses were used to convert the test curves into static curves. Consequently, the obtained test results were free from the influence of the applied strain rate.

3. Numerical investigation

3.1. Finite element (FE) models of SBB T- and X-joints

3.1.1. General

ABAQUS [16] was used to perform the comprehensive FE analyses in this study. The static (general) analysis procedure given in ABAQUS [16] was used as the solver. As the induced strains in the FE models during the applied loads were unidirectional (i.e. no load reversal), the isotropic strain hardening law was selected for the analysis. The von-Mises yield criterion is generally the default criterion used to predict the onset of yielding in most metals, except for porous metals. Therefore, the yielding onsets of FE models in this study were based on the von-Mises yield theory. In the FE analyses, the growth of the time step was kept non-linear to reduce the overall computation time. Furthermore, the default Newton-Raphson method was used to find the roots of non-linear equilibrium equations. The material non-linearity was considered in the FE models by assigning the measured values of static stress-strain curves of flat and corner regions of RHS members in the plastic material definition part of the FE model. However, prior to the inclusions of experimentally obtained constitutive material curves in the FE models, they were first converted into static curves, and then transformed into true stress-strain curves. On the other hand, the geometric non-linearities in FE models were considered by enabling the non-linear geometry parameter (*NLGEOM), which in turn allow FE models to undergo large displacement during the analyses. Furthermore, various factors, including through-thickness division, contact interactions, mesh seed spacing, corner region extension and element types, were also studied and discussed in the following sub-sections of this paper. The labelling of parametric SBB T- and X-joint FE specimens was kept identical to the label system used in the test programs [1,2].

3.1.2. Material properties, mesh seed spacing and element type

The test specimens of the experimental programs [1,2] were fabricated from tubular members that belonged to the same batch of tubes that was used in Pandey and Young [17]. Additionally, Pandey and Young [18] investigated the material properties of welding filler material. The details pertaining to the material properties of welding filler material and tubular members can be referred to Pandey and Young [17,18]. The inclusions of static stress-strain curves in FE models helped avert the influence of strain rate from FE results. The true stress-strain curves of welding filler material as well as flat and corner portions of RHS members were allocated to the corresponding parts of the FE specimens. In this study, the influence of cold-working in RHS members was included in FE models by assigning wider corner regions. Various distances for corner extension in RHS members were considered in the sensitivity analyses, and finally, the corner portions were elongated by $2t$ into the neighbouring flat portions, which was in agreement with other studies conducted on CFHSS tubular members and joints (Pandey et al. [19,20] and Ma et al. [21,22]). Except for the welds, all other parts of the FE models were developed using the C3D20 element. On the other hand, the C3D10 element was used to model the weld parts due to their complicated shapes. The weld parts were freely meshed using the free-mesh algorithm, while brace and chord parts were meshed using the structure-mesh algorithm. The use of solid elements helped in making realistic fusions between tubular and weld parts of SBB T- and X-joints FE models.

Convergence studies were conducted using different mesh sizes, and finally, chord and brace members were seeded at 4 mm and 7 mm intervals, respectively, along both longitudinal and transverse directions. Moreover, the seeding intervals of weld parts reciprocated the seeding spacings of their respective brace parts. In order to ensure the smooth transfer of stresses between the flat portions of the RHS cross-section, the corner portions of the RHS cross-section were split into ten elements. FE analyses were also conducted to examine the influence of divisions along the wall thickness (t) of RHS members. The results of these FE analyses demonstrated the trivial influence of wall thickness divisions on the N vs u curves of the investigated joints. The use of the C3D20 element having one built-in node along the thickness direction as well as the small wall thickness of test specimens (i.e. $t \leq 6$ mm) led to such observations. The presence of a built-in node naturally provides one division along the wall thickness of tubular members (i.e. two layers). It is worth noting that a similar observation was also noticed in other studies (Pandey et al. [19,20] and Crockett [23]). Thus, for the validations of SBB T- and X-joints FE models, the wall thicknesses of tubular members were kept unsplit.

3.1.3. Modelling of welds and contact interactions

Along the longitudinal and transverse directions of an SBB joint, the values of dihedral angle between brace and chord members are equal to 135° and 90°, respectively. Thus, as per the prequalified weld specifications of AWS D1.1M [24], the partial joint penetration (PJP) groove weld and fillet welds were modelled along the longitudinal and transverse directions of SBB T- and X-joints FE specimens. The welds were modelled using the average values of measured weld sizes, which are reported in Pandey and Young [1,2]. The inclusions of weld geometries and weld material properties appreciably improved the overall accuracies of FE models. Further, modelling of weld parts helped attain realistic stress transfer between different parts of the FE model, which facilitated obtaining the actual joint behaviour. The selection of the C3D10 element maintained optimum stiffness around the joint perimeter due to its ability of taking complicated shapes. A total of two types of contact interactions was defined in SBB T- and X-joints FE models, as shown in Figs. 2(a) and 2(b). First, contact interaction between brace and chord members of SBB T- and X-joints FE models. Second, contact interaction between chord members and V-shaped end blocks of SBB T-joint FE models. In addition, a tie constraint was also established between weld and tubular members of SBB T- and X-joints FE models, as shown in Figs. 2(c) and 2(d). Both contact interactions were established using the built-in surface-to-surface contact definition.

The contact interaction(s) between brace and chord members of SBB T- and X-joints FE models was kept frictionless, while a frictional penalty of 0.3 was imposed on the contact interaction between chord member and V-shaped end blocks of SBB T-joint FE models. Along the normal direction of these two contact interactions, a 'hard' contact pressure overclosure was used. In addition, finite sliding was permitted between the interaction surfaces. For contact interactions and tie constraint, the surfaces were connected to each other using the 'master-slave' algorithm technique. This technique permits the separation of fused surfaces under tension, however, it does not allow penetration of fused surfaces under compression. This technique of fusion between various parts of FE models has been successfully used in several other investigations (Pandey et al. [19,20]; Li and Young [25,26]; Li and Young [27,28]). For the brace-chord interaction, the cross-section surface of the brace connected to the chord member was assigned as the 'master' region (relatively less deformable), while the chord connecting surface was assigned as the 'slave' region (relatively more deformable). For the chord member and V-shaped end block interaction, the chord member was assigned as the 'slave' region, while the V end block was assigned as the 'master' region. For the weld-tubular member tie connection, the weld surfaces were assigned as the 'master' regions, while the connecting brace and chord surfaces were assigned as the 'slave' regions.

3.1.4. Boundary conditions

The boundary conditions in SBB T- and X-joints FE models were assigned by creating reference points. Three reference points were created for the SBB T-joint FE model, including one top reference point (TRP) and two bottom reference points (BRP-1 and BRP-2). The TRP replicated the fixed boundary condition of the top brace end, while BRP-1 and BRP-2 replicated the boundary conditions of the roller positioned at each chord end. As shown in Fig. 3(a), the TRP was created at the cross-section centre of the top brace end and BRP-1 and BRP-2 were created at 20 mm below the centre of the bottom surfaces of V-shaped end blocks. The TRP, BRP-1 and BRP-2 were then coupled to their corresponding surfaces using the built-in kinematic coupling type. In order to exactly replicate the boundary conditions of the SBB T-joint test setup, all degrees of freedom (DOF) of TRP were restrained. On the other hand, for BRP-1 and BRP-2, except for the translations along the L_1 and L_0 directions of the FE specimen as well as the rotation about the b_0 direction, the remaining DOF of BRP-1 and BRP-2 were also restrained. In addition, all DOF of other nodes of SBB T-joint FE specimen were kept unrestrained for both rotation and translation.

In SBB X-joint FE model, top and bottom reference points (TRP and BRP) were created at the cross-section centres of their respective braces, as shown in Fig. 3(b). Subsequently, TRP and BRP were coupled to their respective brace end cross-section surfaces using the kinematic coupling type. In order to exactly replicate the boundary conditions of the SBB X-joint test setup, all DOF of TRP were restrained. However, except for the translation along the vertical direction of the SBB X-joint specimen, all other DOF of BRP were also restrained. Moreover, all DOF of other nodes of the SBB X-joint FE specimen were kept unrestrained for both rotation and translation. Using the displacement control method, compression load was then applied at the bottom reference points of the SBB T- and X-joints FE models. In addition, the size of the step increment was kept small in order to obtain smooth load vs chord indentation curves. Following this approach, the boundary conditions and load application in FE models were identical to the test programs [1,2].

3.1.5. Weld heat affected region (WHAR)

The heat transferred to parent tubular members during the welding process has a considerable impact on the overall behaviour of hollow section joints [7,19]. The design rules in international standards/guidelines (AISC 360 [29]; ISO 14346 [30]; IIW [31]; CIDECT [32]; EC3 [33]) are identical for HSS produced from different methods, namely by adding alloying elements and by various heat treatment techniques. However, it has been reported in some recent studies (Pandey and Young [7]; Stroetmann et al. [34]; Javidan et al. [35]; Amraei et al. [36,37]) that HSS produced by different methods exhibited different extents of softening around the welds. Investigations carried out by Stroetmann et al. [34], Javidan et al. [35] and Amraei et al. [36,37] reported 16% to 32% reductions in the ultimate strengths of S960 steel grade parent materials around the welds. The material properties of the weld heat affected region (WHAR) of tubular joints having nominal 0.2% proof stress of 960 MPa and wall thicknesses between 3 mm to 6 mm were investigated by Pandey and Young [7]. A 14% to 32% reduction in the ultimate strengths of the parent metals was reported by Pandey and Young [7] in the first 6 mm distance of the heat affected zone. The definition of WHAR for tubular joints was proposed by Pandey et al. [19], as shown in Fig. 4. For SBB T- and X-joints FE models, the spreads of WHAR are shown in Figs. 3(a) and 3(b), respectively. In addition, a simplified strength reduction (S_{rl}) model was proposed by Pandey et al. [19] for S900 and S960 steel grades tubular joints to integrate the material properties of WHAR in FE models, as illustrated in Fig. 5. The proposed strength reduction model was successfully used to perform the numerical investigation and design of CFHSS T- and TF-joints (Pandey et al. [19,20]). Therefore, it was also included in this investigation, and accordingly, material properties were assigned to the WHAR of SBB T- and X-joints FE models. The adoption of WHAR appreciably improved the accuracies of FE models and, thus, the numerical results.

3.2. Validations of SBB T- and X-joints FE models

The modelling approaches described in the preceding section of this paper were used to develop SBB T- and X-joints FE models. The test results of SBB T- and X-joints reported in Pandey and Young [1,2] were used to validate their corresponding FE models. The validations were performed by comparing the N_f, N_{max}, load vs chord indentation histories and failure modes of test and FE specimens. The measured dimensions of tubular members and welds were used to develop all SBB T- and X-joints FE models. In addition, measured material properties of tubular members, welds and WHAR were also included. The N_f and N_{max} of test specimens were compared with those predicted from their corresponding FE models ($N_{f,FE}$ and $N_{max,FE}$), as shown in Tables 1 and 2, respectively. Referring to Table 1, when the joint failure strengths of SBB T-joint ($N_{f,T}$) test specimens were compared with the strengths predicted from SBB T-joint FE models, the mean (P_m) and coefficients of variation (COV) (V_p) of the comparisons were 0.97 and 0.031, respectively. However, when the ultimate capacities of SBB T-joint ($N_{max,T}$) test specimens were compared with the FE strengths, the P_m and V_p of the comparisons were 1.01 and 0.010, respectively.

On the other hand, as presented in Table 2, when the joint failure strengths of SBB X-joint ($N_{f,X}$)

test specimens were compared with the strengths predicted from SBB X-joint FE models, the P_m and V_p of the comparisons were 0.99 and 0.018, respectively. However, when the ultimate capacities of SBB X-joint ($N_{max,X}$) test specimens were compared with the FE strengths, the P_m and V_p of the comparisons were 1.00 and 0.013, respectively. Likewise in the experimental investigation, the N_f of investigated SBB joints was determined by jointly considering the ultimate capacity and ultimate deformation limit (i.e. $0.03b_0^{'}$) loads, whichever occurred earlier in the N vs u curves. Figs. 6 and 7 respectively present the comparisons of N vs u curves between typical SBB T- and X-joints test and FE specimens. Moreover, Figs. 8 and 9 present the comparisons of failure modes between typical SBB T- and X-joints test and FE specimens, respectively. Therefore, from Tables 1-2 and Figs. 6-9, it can be concluded that the validated FE models precisely replicated the overall static behaviour of SBB T- and X-joints.

3.3. Parametric study

3.3.1. Introduction

The test results reported in Pandey and Young [1,2] were not sufficient to develop a broad understanding of various governing factors affecting the static performance of CFHSS SBB T- and X-joints subjected to compression loads. Therefore, the data pool was widened by performing a comprehensive numerical parametric study using the validated SBB T- and X-joints FE models. In total, 200 parametric FE analyses were performed in this study, including 100 SBB T-joints and 100 SBB X-joints. Table 3 presents the ranges of various critical parameters considered in the numerical parametric study. All FE modelling techniques used in the validations of SBB T- and X-joints were also employed in the parametric study. It is important to mention that the N_f of all SBB FE specimens were controlled by the ultimate deformation limit (i.e. $0.03b_0^{'}$) loads.

3.3.2. Details of parametric FE modelling

In the numerical investigation, the dimensions of tubular members included practical sizes. Overall, the values of cross-section width and depth of braces and chords of parametric FE specimens varied between 50 mm to 200 mm, while wall thickness of braces and chords varied between 2.5 mm to 12 mm. The R_1 and R_0 of RHS conformed to the commercially produced HSS members (SSAB [38]). In this study, R_1 and R_0 were kept as $2t$ for $t \leq 6$ mm, $2.5t$ for $6 < t \leq 10$ mm and $3t$ for $t > 10$ mm, which in turn also meet the limits detailed in EN 10219-2 [39]. The L_1 and L_0 of SBB T- and X-joints FE specimens were determined using the formulae that were also used to design the test specimens [1,2]. For meshing along the longitudinal and transverse directions of RHS members, seedings were approximately spaced at the minimum of $b/30$ and $h/30$, where b and h stand for cross-section width and depth of the RHS member. Overall, the adopted mesh sizes of parametric FE specimens varied between 3 mm to 10 mm. On the other hand, the seeding interval of weld parts of parametric FE specimens reciprocated the seeding interval of their corresponding brace parts. For precise replication of RHS curvatures, the corner portions of braces and chords were split into ten parts. Likewise, in the validation process, the corner portions of braces and chords were elongated by $2t$ into their neighbouring flat portions. For RHS members with $t \leq 6$ mm, no divisions were made along the wall thickness of braces and chords. However, for RHS members with $t > 6$ mm, the wall thickness of braces and chords was divided into two layers.

For SBB T- and X-joints FE specimens, the leg size of fillet weld as well as projected weld lengths of PJP groove weld were designed as 1.5 times the minimum of t_1 and t_0, which also meet the minimum requirements given in AWS D1.1M [24] for prequalified tubular joints. The weld designs of both SBB T- and X-joints FE specimens were consistent with the experimental programs [1,2]. In the parametric study, the material properties of flat and corner portions of RHS 150×150×6 were assigned to the flat and corner portions of braces and chords of FE specimens. Besides, weld parts of all SBB T- and X-joints parametric FE specimens were given the measured material properties of welding filler material. Table 4 presents the measured material properties of RHS 150×150×6 and welding filling material adopted in the parametric study, which include Young's modulus (E), 0.2% proof stress and strain ($\sigma_{0.2}$ and $\varepsilon_{0.2}$), ultimate stress and strain (σ_u and ε_u), fracture strain (ε_f) and Ramberg-Osgood parameter (n). On the other hand, the material properties and spread of WHAR were in accordance with the recommendations proposed by Pandey et al. [19].

3.3.3. Failure mode of SBB T- and X-joints

The load transfer mechanism of SBB T- and X-joints is different to those of traditional RHS T- and X-joints. In SBB joints, the flat regions of the connected brace member(s) get inter-locked with the chord corner edge(s). The axial load in SBB joints first transferred from brace member to the chord crown locations and then to the chord saddle locations. Subsequently, the whole joint region locally deformed. The brace connected chord corner edge(s) is work-hardened and has high out-of-plane bending stiffness compared to the adjacent flat regions. In addition, unlike CHS joints, the chord saddle regions of SBB joints extend on the complete cross-section depth (h_1) of the brace member. As a result, generally, SBB joints have enhanced ultimate strength and superior deformation capacity compared to their traditional counterparts. In this investigation, all SBB T- and X-joints demonstrated good deformation capacity both before and after the peak load. The post-peak load dropped gradually and was accompanied by no punching at the chord connecting regions. Generally, all SBB T- and X-joints have shown peak load at sufficiently large values of chord crown indentation. The initial stiffness and joint ultimate capacities of SBB T- and X-joints increased as β' ratio increased and 2γ ratio decreased.

All SBB T- and X-joints test [1,2] and FE specimens were failed by chord crown failure mode, which was denoted by the letter 'C' in this paper. In the chord crown failure (C) mode, the test and FE specimens were failed by predominant convex deformation at the crown locations of the chords. It is important to note that this failure mode was defined corresponding to the N_f of SBB T- and X-joints, which in turn was computed by combinedly considering the ultimate capacity and deformation limit loads, whichever occurred earlier in the N vs u curve. It is important to mention that the convex deformation at the crown locations of all SBB test and FE specimens was always larger than the corresponding concave deformation at the saddle locations. The predominance of deformation at crown location remained valid for both N_f and N_{max} of SBB T- and X-joints test and FE specimens. The attainment of N_{max} of test and FE specimens was accompanied by large deformation at the chord crown and saddle regions. Generally, the N vs u curves of SBB T- and X-joints test and FE specimens entered a stagnant phase near the N_{max}, followed by a very gradual load drop in the post-ultimate regions. In this study, for all SBB T- and X-joints, the loads corresponding to the 3% deformation limit criterion occurred much earlier than their corresponding peak loads, and thus, governed the joint failure resistances. This highlights the fact that SBB T- and X-joints possess sufficient strength reserve to attain their respective ultimate capacities. Moreover, global buckling was not observed in the brace members of test and FE specimens. In this investigation, the specimens were failed by the C mode for $0.22 \leq \beta' \leq 0.70$.

4. Existing design provisions

Presently, design provisions of SBB joints are not included in any code of practice. In the literature, design rule is only available for Q235 steel grade SBB T-joint (Cheng and Wang [13]). Generally, the static response of T- and X-joints undergoing compression load via braces remains similar. Therefore, in this study, the N_f and N_{max} of both SBB T- and X-joints test and parametric FE specimens were evaluated against the nominal strengths predicted from the design equation proposed by Chen and Wang [13]. Moreover, the SBB joint configuration partially resembles to that of conventional RHS-to-RHS (due to orientation of brace) and CHS-to-CHS (due to orientation of chord) configurations. Thus, the N_f and N_{max} of test and parametric FE specimens were also evaluated against the nominal strengths of RHS-to-RHS and CHS-to-CHS T- and X-joints design rules given in EC3 [33]. The nominal strengths were calculated using the measured values of RHS members dimensions and material properties. Under axial compression load via braces, SBB T-joints were subjected to chord-in-plane bending. In this investigation, the effect of normal stresses developed due to chord-in-plane bending on the static strengths of SBB T-joints was considered through the chord stress function (Q_f). On the other hand, in this study, no preload was applied to the chord members of SBB X-joints. Therefore, the values of k_n and Q_f were set to unity in Eqs. (1) to (5) for SBB X-joints. The design equations given in Chen and Wang [13] were developed for Q235 steel grade SBB T-joints, thus, nominal strengths predicted from Chen and Wang [13] were multiplied by C_f=0.80 to facilitate their evaluations against the test and FE strengths of CFHSS SBB T- and X-joints. The comparison results for SBB T- and X-joints are presented in Tables 5 and 6, respectively.

4.1. Chen and Wang [13]

Chen and Wang [13] proposed a design equation (Eq. (1)) to predict the ultimate capacity of an SBB T-joint undergoing compression load via brace member. The chord ends of the SBB T-joint were supported by pins. The steel grade of test specimens was Q235 with the yield strength of 235 MPa.

$$N_{CW} = 1.736\beta^{\frac{1}{2}}\gamma^{\frac{1}{2}}\tau^{\frac{1}{6}}\left(\frac{1-\beta}{k_n}\right)\left[Q_f\,\frac{f_{y0}t_0^2}{\sin\theta_1}\left(\frac{2\beta}{(1-\beta)\sin\theta_1}+\frac{4}{\sqrt{1-\beta}}\right)/\gamma_{M5}\right] \quad (1)$$

In order to prolong the suitability of Eq. (1) for CFHSS SBB joints, C_f=0.80 should be included in Eq. (1). After including the C_f factor in Eq. (1), the nominal strength was represented by $\hat{N}_{CW}$. In Eq. (1), chord yield strength is denoted by f_{y0}, partial safety factor of tubular joints given in EC3 [33] is denoted by γ_{M5} and the angle between brace and chord members is denoted by θ_1.

4.2. Eurocode 3 [33]

The design provisions given in EC3 [33] are applicable for tubular joints with steel grades up to S700. However, a material factor (C_f) is required to be multiplied to the design rules when steel grade exceeds S355. When steel grade ranged between 550 to 700 MPa, the value of material factor (C_f) is equal to 0.80. Furthermore, EC3 [33] explicitly recommended the value of partial safety factor for tubular joints (γ_{M5}) equal to 1.0.

- For RHS-to-RHS T- and X-joints:

<u>Chord face failure:</u>

$$\hat{N}_{E,RR} = \frac{C_f}{\gamma_{M5}}Q_f\,\frac{f_{y0}t_0^2}{\sin\theta_1}\left(\frac{2\eta}{(1-\beta)\sin\theta_1}+\frac{4}{\sqrt{1-\beta}}\right) \quad (2)$$

<u>Chord side wall failure:</u>

$$\hat{N}_{E,RR} = \frac{Q_f}{\gamma_{M5}}\,\frac{f_b t_0}{\sin\theta_1}\left(\frac{2h_1}{\sin\theta_1}+10t_0\right) \quad (3)$$

- For CHS-to-CHS T- and X-joints:

<u>For CHS-to-CHS T-joints:</u>

$$N^{\wedge}_{E,CC} = \frac{C_f}{\gamma_{M5}}\left[Q_f \frac{f_{y0}t_0^2}{\sin\theta_1}\left(2.6+17.7\left(\beta'\right)^2\right)\gamma^{0.2}\right] \quad (4)$$

<u>For CHS-to-CHS X-joints:</u>

$$N^{\wedge}_{E,CC} = \frac{C_f}{\gamma_{M5}}\left[Q_f \frac{f_{y0}t_0^2}{\sin\theta_1}\left(\frac{2.6+2.6\beta'}{1-0.7\left(\beta'\right)}\right)\gamma^{0.15}\right] \quad (5)$$

In Eqs. (2) and (3), the term η is equal to h_1/b_0 and f_b represents buckling stress of chord member. The effect of chord stress on the joint strength was determined using the chord stress function (Q_f) as shown below:

$$Q_f = (1-|n|)^{(0.6-0.5\beta)} \quad (6)$$

In this study, no external axial force was applied on chord members, therefore the value of N_0 is equal to zero in Eqs. (7) and (8). However, as T-joints were supported on rollers, the chord members were subjected to simply supported bending moment (M_0) at the brace-chord intersection, which is equal to $0.25N_1(L_0\text{-}h_1)$. In Eq. (6), the chord stress factor (n) can be calculated as follows:

For class 1 and 2 sections:

$$n = \frac{N_0}{N_{pl,0}} + \frac{M_0}{M_{pl,0}} = \frac{0.25N_1\left(L_0-h_1\right)}{W_{pl,0}\times f_{y0}} \quad \text{(as, } N_0\text{=0)} \quad (7)$$

For class 3 sections:

$$n = \frac{N_0}{N_{el,0}} + \frac{M_0}{M_{el,0}} = \frac{0.25N_1\left(L_0-h_1\right)}{W_{el,0}\times f_{y0}} \quad \text{(as, } N_0\text{=0)} \quad (8)$$

where $W_{pl,0}$ and $W_{el,0}$ are plastic and elastic section moduli of chord member, respectively; and N_1 is the joint strength.

5. Reliability analysis

In order to examine the reliability of existing and proposed design equations, a reliability study was performed as per AISI S100 [40]. Eq. (9) was used to calculate the reliability index (β_0). In this investigation, a lower bound value of 2.50 was taken as the target β_0. Therefore, when $\beta_0 \geq 2.50$, the design equation was treated as reliable in this study.

$$\beta_0 = \frac{\ln(C_\phi M_m F_m P_m / \phi)}{\sqrt{V_M^2 + V_F^2 + C_P V_P^2 + V_Q^2}} \tag{9}$$

A dead load (DL)-to-live load (LL) ratio of 0.20 was used to compute the calibration coefficient (C_ϕ) in Eq. (9). For the material factor, the mean value and COV were respectively symbolised by M_m and V_M. For the fabrication factor, the mean value and COV were respectively symbolised by F_m and V_F. Referring to AISI S100 [40], the M_m and V_M were adopted as 1.10 and 0.10, respectively. Additionally, F_m and V_F were adopted as 1.00 and 0.10, respectively. The resistance factor required to convert the nominal strength to design strength was denoted by ϕ. The mean value of ratios of test and FE strengths-to-nominal strengths predicted from literature and code was denoted by P_m, while the corresponding COV was denoted by V_P. The correction factor (C_P) proposed by AISI S100 [40] was also used in Eq. (9) to incorporate the effect of the number of data under consideration. Besides, V_Q symbolised the COV of load effects. In order to evaluate the reliability levels of EC3 [33] design provisions, the DL and LL were combined as 1.35DL + 1.5LL as per EN [41], and thus, the calculated value of C_ϕ was 1.463. Further, to examine the reliability levels of the design equation proposed by Chen and Wang [13] as well as for the proposed design rules, the DL and LL were combined as 1.2DL + 1.6LL as per ASCE 7 [42], and the calculated value of C_ϕ was 1.521.

6. Comparisons of joint failure strengths and ultimate capacities with existing design rules

The comparisons of N_f and N_{max} of SBB T- and X-joints test and FE specimens with nominal strengths are shown in Tables 5 and 6, respectively. The comparisons are also graphically shown in Figs. 10 and 11. Table 5 presents the comparisons of $N_{f,T}$ and $N_{max,T}$ of SBB T-joint test and parametric FE specimens with nominal strengths predicted from Chen and Wang [13] and EC3 [33]. The comparisons results proved that Chen and Wang [13] design equation satisfactorily predicted the $N_{f,T}$ of cold-formed S960 steel grade SBB T-joints. However, the predictions were quite dispersed, and the design equation failed to meet the minimum value of target β_0. On the other hand, the comparisons of predictions of RHS-to-RHS and CHS-to-CHS T-joint design rules of EC3 [33] with $N_{f,T}$ of SBB T-joints were found to be very conservative, largely dispersed and unreliable. From the comparisons of $N_{max,T}$ of SBB T-joint test and parametric FE specimens with nominal strengths, it can be noticed that the predictions from Chen and Wang [13] design equation were quite conservative. In addition, for $N_{max,T}$ of SBB T-joints, RHS-to-RHS and CHS-to-CHS T-joint design rules of EC3 [33] were found to be highly conservative and largely dispersed. Figs. 10(a) and 10(b) graphically present the comparisons of $N_{f,T}$ and $N_{max,T}$ of SBB T-joint test and parametric FE specimens with nominal strengths predicted from Chen and Wang [13] and CHS-to-CHS T-joint design rule of EC3 [33], respectively.

The comparisons of $N_{f,X}$ and $N_{max,X}$ of SBB X-joint test and parametric FE specimens with nominal strengths predicted from Chen and Wang [13] and EC3 [33] are presented in Table 6. The predictions from Chen and Wang [13] design equation were found to be quite unconservative, largely dispersed and unreliable for $N_{f,X}$ of SBB X-joints. On the contrary, the RHS-to-RHS X-joint design rule of EC3 [33] satisfactorily predicted the $N_{f,X}$ of cold-formed S960 steel grade SBB X-joints. However, the predictions were quite dispersed, and the design rule was found to be unreliable. On the other hand, the comparisons of predictions of CHS-to-CHS X-joint design rule of EC3 [33] with $N_{f,X}$ of SBB X-joints were found to be quite conservative, dispersed and unreliable. With regard to the comparisons with $N_{max,X}$ of SBB X-joints, Chen and Wang [13] design equation satisfactorily predicted the $N_{max,X}$ of cold-formed S960 steel grade SBB X-joints, however, the predictions were quite scattered and overall, the design rule was found to be unreliable. On the contrary, the comparisons of predictions of RHS-to-RHS and CHS-to-CHS X-joint design rules of EC3 [33] with $N_{max,X}$ of SBB X-joints were found to be very conservative and uneconomical. Figs. 11(a) and 11(b) graphically present the comparisons of $N_{f,X}$ and $N_{max,X}$ of SBB X-joint test and parametric FE specimens with nominal strengths predicted from Chen and Wang [13] and CHS-to-CHS X-joint design rule of EC3 [33], respectively.

In order to propose design equation for SBB T-joints, correction factors based on critical geometric ratios were applied by Chen and Wang [13] on chord face failure design equation of conventional RHS-to-RHS T-joint given in CIDECT [32]. It is important to note that the load transfer path and failure mode of SBB T- and X-joints were quite different to those of conventional RHS-to-RHS T-joint. Therefore, the use of RHS T-joint design rule for SBB T-joint could lead to inaccurate joint strengths. Further, it is essential to note that Chen and Wang [13] design equation was developed for SBB T-joints made of Q235 steel. The COV of the design equation (Eq. (1)) was 20.6% [13], which in turn revealed that the predictions of Eq. (1) were quite dispersed even for the investigated Q235 steel grade SBB T-joints. Owing to (1-β) factor in Eq. (1), the strength of the SBB T-joint decreased as β increased, which is opposite to the static behaviour of SBB joints. Moreover, the effect of chord-in-plane bending was considered using functions present in both the numerator and denominator of Eq. (1), which eventually eliminated the total chord-in-plane bending influence from the joint strength. These shortcomings could be the possible reasons behind the inaccuracies of Chen and Wang [13] design equation.

Overall, RHS-to-RHS and CHS-to-CHS T- and X-joints design rules of EC3 [33] were found to be quite conservative for the N_f and N_{max} of cold-formed S960 steel grade SBB T- and X-joints. One of the primary reasons could be the enhanced strengths of SBB T- and X-joints due to the rotation of chord members. In addition, SBB configuration also prevents the early bending (for joints with small β ratio) and buckling (for joints with large β ratio) of chord flat regions, which also lead to increased static strengths compared to their corresponding conventional RHS-to-RHS and CHS-to-CHS T- and X-joints.

7. Proposed design rules

In order to predict the N_f and N_{max} of cold-formed S960 steel grade SBB T- and X-joints, design rules are proposed in this study by two design approaches. Under the first design approach, named as proposal-1, new design equations are proposed to predict the N_f and N_{max} of SBB T- and X-joints. Under the second design approach, named as proposal-2, the N_f and N_{max} of SBB T- and X-joints were predicted by applying correction factor(s) on RHS-to-RHS and CHS-to-CHS joints design rules (Eqs. (2), (4) and (5)) given in EC3 [33]. The design equations proposed in this study are derived using the regression analyses and based on the minimum scatter approach. The influences of governing geometric parameters on the static strengths of SBB T- and X-joints were carefully considered. Furthermore, as welds were modelled in all parametric FE specimens, the effects of weld and associated WHAR were implicitly included in the proposed design equations. In order to calculate design strengths (N_d), the proposed nominal strengths (N_{pn1}, N_{pn2} and N_{pn3}) in the following sub-sections of this paper shall be multiplied by their correspondingly recommended resistance factors (ϕ), i.e. $N_d = \phi$ (N_{pn1} or N_{pn2} or N_{pn3}). All design rules proposed in this study are valid for $0.30 \leq \beta \leq 0.90$, $0.22 \leq \beta' \leq 0.70$, $16.6 \leq 2\gamma \leq 40$ and $0.50 \leq \tau \leq 1.28$. As all SBB T- and X-joints specimens were failed by the C mode, the proposed design equations are only valid for this failure mode.

7.1. SBB T-joints

7.1.1. For joint failure strength

The parameters β', 2γ and τ demonstrated a significant influence on the $N_{f,T}$ of SBB T-joints that failed by the C mode. Under proposal-1, a new design equation (Eq. (10)) has been proposed to predict the $N_{f,T}$ of CFHSS SBB T-joint that failed by the C mode by taking into consideration the effect of important geometric factors as well as P_m and V_p of the overall comparison. Under proposal-2, correction factor based on β' is applied on the current RHS-to-RHS and CHS-to-CHS T-joints design rules given in EC3 [33], as shown in Eqs. (11) and (12).

<u>Proposal-1:</u>

$$N_{pn1} = \frac{f_{y0} t_0^2 \left(1.5\beta' + 0.6\right)\left(\tau + 9\right)}{\left[1.2 - 0.002\left(2\gamma\right)\right]} \tag{10}$$

<u>Proposal-2:</u>

(a) Using RHS-to-RHS T-joint design rule of EC3 [33]:

$$N_{pn2} = (2.5 - 2.7\beta') N^{\wedge}_{E,RR} \tag{11}$$

(b) Using CHS-to-CHS T-joint design rule of EC3 [33]:

$$N_{pn3} = (2.3 - 2.1\beta') N^{\wedge}_{E,CC} \tag{12}$$

The terms $N^{\wedge}_{E,RR}$ and $N^{\wedge}_{E,CC}$ in Eqs. (11) and (12) can be obtained from Eqs. (2) and (4), respectively. As shown in Table 5, the P_m and V_p of proposal-1 (Eq. (10)) are 1.01 and 0.103, respectively. The P_m and V_p of proposal-2(a) (Eq. (11)) are 1.02 and 0.124, respectively. The P_m and V_p of proposal-2(b) (Eq. (12)) are 1.01 and 0.115, respectively. For Eqs. (10), (11) and (12), ϕ equal to 0.85, 0.80 and 0.80 were recommended, resulting in β_0 equal to 2.53, 2.67 and 2.68, respectively. Thus, Eqs. (10), (11) and (12) must be multiplied by ϕ equal to 0.85, 0.80 and 0.80, respectively, to get their corresponding design strengths (N_d). The comparisons of $N_{f,T}$ of test and FE specimens with nominal strengths predicted from Chen and Wang [13], CHS-to-CHS T-joint design rule of EC3 [33] and proposal-1 are graphically presented in Fig. 10(a). In addition, the distributions of the ratios of $N_{f,T}$ of test and FE specimens-to-nominal strengths predicted from Eqs. (1) to (4) and Eq. (10) are shown in Fig. 12. Compared to the design provisions given in Chen and Wang [13] and EC3 [33], the predictions from Eqs. (10), (11) and (12) are relatively more accurate, less dispersed and reliable.

7.1.2. For joint ultimate capacity

The $N_{max,T}$ of CFHSS SBB T-joints that failed by the C mode were also considerably influenced by β', 2γ and τ parameters. A new design equation (Eq. (13)) is proposed, under proposal-1, to predict the $N_{max,T}$ of CFHSS SBB T-joint that failed by the C mode by taking into consideration the effect of important geometric factors as well as P_m and V_p of the overall comparison. Under proposal-2, as shown in Eqs. (14) and (15), correction factor based on β' is applied on the current RHS-to-RHS and CHS-to-CHS T-joints design rules given in EC3 [33].

<u>Proposal-1:</u>

$$N_{pn1} = \frac{f_{y0} t_0^2 \left(1.7\beta' + 0.7\right)\left(\tau + 7\right)}{\left[1.1 - 0.01\left(2\gamma\right)\right]} \tag{13}$$

<u>Proposal-2:</u>

(a) Using RHS-to-RHS T-joint design rule of EC3 [33]:

$$N_{pn2} = \left[2 + 1.65\beta' - 5\left(\beta'\right)^2\right] N_{E,RR}^{\wedge} \tag{14}$$

(b) Using CHS-to-CHS T-joint design rule of EC3 [33]:

$$N_{pn3} = (2.8 - 2.4\beta') N_{E,CC}^{\wedge} \tag{15}$$

The terms $N_{E,RR}^{\wedge}$ and $N_{E,CC}^{\wedge}$ in Eqs. (14) and (15) can be obtained from Eqs. (2) and (4), respectively. As shown in Table 5, the P_m and V_p of proposal-1 (Eq. (13)) are 1.02 and 0.104, respectively. The P_m and V_p of proposal-2(a) (Eq. (14)) are 1.03 and 0.151, respectively. The P_m and V_p of proposal-2(b) (Eq. (15)) are 1.00 and 0.095, respectively. For Eqs. (13), (14) and (15), ϕ equal to 0.85, 0.80 and 0.85 were recommended, resulting in β_0 equal to 2.53, 2.58 and 2.50, respectively. Thus, Eqs. (13), (14) and (15) must be multiplied by ϕ equal to 0.85, 0.80 and 0.85, respectively, to get their corresponding design strengths (N_d). The comparisons of $N_{max,T}$ of test and FE specimens with nominal strengths predicted from Chen and Wang [13], CHS-to-CHS T-joint design rule of EC3 [33] and proposal-1 are graphically presented in Fig. 10(b). In addition, the distributions of the ratios of $N_{max,T}$ of test and FE specimens-to-nominal strengths predicted from Eqs. (1) to (4) and Eq. (13) are shown in Fig. 13. Compared to the design provisions given in Chen and Wang [13] and EC3 [33], the predictions from Eqs. (13), (14) and (15) are relatively more accurate, less dispersed and reliable.

7.2. SBB X-joints

7.2.1. For joint failure strength

For SBB X-joints that failed by the C mode, the parameters β', 2γ and τ showed a notable effect on the $N_{f,X}$. Under proposal-1, a new design equation (Eq. (16)) is proposed to predict the $N_{f,X}$ of CFHSS SBB X-joint that failed by the C mode by taking into consideration the effect of important geometric factors as well as P_m and V_p of the overall comparison. Under proposal-2, correction factors based on β' and 2γ are applied on the current RHS-to-RHS and CHS-to-CHS X-joints design rules given in EC3 [33], as shown in Eqs. (17) and (18).

<u>Proposal-1:</u>

$$N_{pn1} = \frac{f_{y0} t_0^2 \left(2\beta' + 0.5\right)\left(0.1\tau + 7\right)}{\left[0.6 + 0.02\left(2\gamma\right)\right]} \tag{16}$$

<u>Proposal-2:</u>

(a) Using RHS-to-RHS X-joint design rule of EC3 [33]:

$$N_{pn2} = \left[1.5 + 1.4\beta' - 3.7\left(\beta'\right)^2\right]\left[1.2 - 0.015\left(2\gamma\right)\right] N_{E,RR}^{\wedge} \tag{17}$$

(b) Using CHS-to-CHS X-joint design rule of EC3 [33]:

$$N_{pn3} = (1.7 - 0.65\beta')\left[1.5 - 0.02\left(2\gamma\right)\right] N_{E,CC}^{\wedge} \tag{18}$$

The terms $N_{E,RR}^{\wedge}$ and $N_{E,CC}^{\wedge}$ in Eqs. (17) and (18) can be obtained from Eqs. (2) and (5), respectively. As shown in Table 6, the P_m and V_p of proposal-1 (Eq. (16)) are 1.00 and 0.109, respectively. The P_m and V_p of proposal-2(a) (Eq. (17)) are 0.99 and 0.069, respectively. The P_m and

V_p of proposal-2(b) (Eq. (18)) are 0.99 and 0.118, respectively. For Eqs. (16), (17) and (18), ϕ equal to 0.80, 0.85 and 0.80 were recommended, resulting in β_0 equal to 2.67, 2.52 and 2.60, respectively. Thus, Eqs. (16), (17) and (18) must be multiplied by ϕ equal to 0.80, 0.85 and 0.80, respectively, to get their corresponding design strengths (N_d). The comparisons of $N_{f,X}$ of test and FE specimens with nominal strengths predicted from Chen and Wang [13], CHS-to-CHS X-joint design rule of EC3 [33] and proposal-1 are graphically presented in Fig. 11(a). In addition, the distributions of the ratios of $N_{f,X}$ of test and FE specimens-to-nominal strengths predicted from Eqs. (1)-(3), (5) and (16) are shown in Fig. 14. Compared to the design provisions given in Chen and Wang [13] and EC3 [33], the predictions from Eqs. (16), (17) and (18) are relatively more accurate, less dispersed and reliable.

7.2.2. For joint ultimate capacity

The $N_{max,X}$ of CFHSS SBB X-joints that failed by the C mode were also substantially affected by β', 2γ and τ parameters. A new design equation (Eq. (19)) is proposed, under proposal-1, to predict the $N_{max,X}$ of CFHSS SBB X-joint that failed by the C mode by taking into consideration the effect of important geometric factors as well as P_m and V_p of the overall comparison. Under proposal-2, correction factors based on β' and 2γ are applied on the current RHS-to-RHS and CHS-to-CHS X-joints design rules given in EC3 [33], as shown in Eqs. (20) and (21).

<u>Proposal-1:</u>

$$N_{pn1} = \frac{f_{y0} t_0^2 \left(2\beta' + 0.5\right)\left(0.5\tau + 8\right)}{\left[1.1 - 0.003\left(2\gamma\right)\right]} \tag{19}$$

<u>Proposal-2:</u>

(a) Using RHS-to-RHS X-joint design rule of EC3 [33]:

$$N_{pn2} = \left[1.5 + 2\beta' - 5\left(\beta'\right)^2\right]\left[1 + 0.003\left(2\gamma\right)\right] N_{E,RR}^{\wedge} \tag{20}$$

(b) Using CHS-to-CHS X-joint design rule of EC3 [33]:

$$N_{pn3} = (2 - 0.7\beta')\left[1 + 0.001\left(2\gamma\right)\right] N_{E,CC}^{\wedge} \tag{21}$$

The terms $N_{E,RR}^{\wedge}$ and $N_{E,CC}^{\wedge}$ in Eqs. (20) and (21) can be obtained from Eqs. (2) and (5), respectively. As shown in Table 6, the P_m and V_p of proposal-1 (Eq. (19)) are 1.02 and 0.102, respectively. The P_m and V_p of proposal-2(a) (Eq. (20)) are 1.02 and 0.124, respectively. The P_m and V_p of proposal-2(b) (Eq. (21)) are 1.02 and 0.109, respectively. For Eqs. (19), (20) and (21), ϕ equal to 0.85, 0.80 and 0.85 were recommended, resulting in β_0 equal to 2.56, 2.67 and 2.52, respectively. Thus, Eqs. (19), (20) and (21) must be multiplied by ϕ equal to 0.85, 0.80 and 0.85, respectively, to get their corresponding design strengths (N_d). The comparisons of $N_{max,X}$ of test and FE specimens with nominal strengths predicted from Chen and Wang [13], CHS-to-CHS X-joint design rule of EC3 [33] and proposal-1 are graphically presented in Fig. 11(b). In addition, the distributions of the ratios of $N_{max,X}$ of test and FE specimens-to-nominal strengths predicted from Eqs. (1)-(3), (5) and (19) are shown in Fig. 15. Compared to the design provisions given in Chen and Wang [13] and EC3 [33], the predictions from Eqs. (19), (20) and (21) are relatively more accurate, less dispersed and reliable.

7.3. Unified design equation

The formats of the new design equations proposed in this study (i.e. Eqs. (10), (13), (16) and (19)) to predict the N_f and N_{max} of CFHSS SBB T- and X-joints are identical. Therefore, an attempt has been made to propose a unified design equation to predict the N_f and N_{max} of cold-formed S960 steel grade SBB T- and X-joints that failed by the C mode. The proposed unified design equation, as shown in Eq. (22), is valid for $0.22 \le \beta' \le 0.70$. The values of coefficients (A to F) are given in Table 7.

$$N_{pn1} = f_{y0} t_0^2 \frac{\left(\mathrm{A}\beta' + \mathrm{B}\right)\left(\mathrm{C}\tau + \mathrm{D}\right)}{\left[\mathrm{E} + \mathrm{F}\left(2\gamma\right)\right]} \qquad (22)$$

8. Conclusions

This study presents a comprehensive numerical investigation and design of cold-formed S960 steel grade square bird-beak (SBB) T- and X-joints. Accurate finite element (FE) models of SBB T- and X-joints were developed in this study using the test results obtained from Pandey and Young [1,2]. An extensive FE parametric study was then performed, which comprised 100 SBB T-joints and 100 SBB X-joints. The welds and associated weld heat affected regions were included in all FE parametric models, which appreciably improved the accuracy of numerical results. In this investigation, the ultimate deformation limit criterion controlled the joint failure strengths (N_f) of all SBB T- and X-joints. Moreover, the ultimate capacities of all SBB T- and X-joints were accompanied by a stagnant phase in their corresponding load vs chord indentation curves, followed by a gradual reduction of load in their post-ultimate regions.

All the SBB T- and X-joints were failed by chord crown failure (C) mode, which was characterised by a visible convex deformation at the crown locations of chord members. The design rules given in Chen and Wang [13] and EC3 [33] are unsuitable and uneconomical for the investigated SBB T- and X-joints. As a result, accurate, less dispersed, user-friendly and reliable design equations are proposed, by two design approaches, to predict the joint failure strengths and ultimate capacities of cold-formed S960 steel grade SBB T- and X-joints that failed by the chord crown failure (C) mode. Under the first design approach (i.e. proposal-1), new design equations are proposed by the authors for cold-formed S960 steel grade SBB T- and X-joints. However, under the second design approach (i.e. proposal-2), the design rules are proposed by applying correction factor(s) on RHS-to-RHS and CHS-to-CHS T- and X-joints design rules given in EC3 [33]. In addition, using the new design equations proposed in this study, a unified design equation has also been proposed to predict the static joint failure strengths and ultimate capacities of the investigated SBB T- and X-joints. The design equations proposed in this study are valid for $0.30 \leq \beta \leq 0.90$, $0.22 \leq \beta' \leq 0.70$, $16.6 \leq 2\gamma \leq 40$ and $0.50 \leq \tau \leq 1.28$.

Acknowledgement

The work described in this paper was fully supported by a grant from the Research Grants Council of the Hong Kong Special Administrative Region, China (PolyU 15218720).

References

[1] Pandey M and Young B. Ultimate Resistances of Member-Rotated Cold-Formed High Strength Steel Tubular T-Joints under Compression Loads, Engineering Structures 2021;244:112601.

[2] Pandey M and Young B. Effect of Member Orientation on the Static Strengths of Cold-Formed High Strength Steel Tubular X-Joints, Thin-walled Structures 2022;170:108501.

[3] Pandey M and Young B. Stress Concentration Factors of Cold-Formed High Strength Steel Tubular T-Joints, Thin-walled Structures 2021;166:107996.

[4] Pandey M and Young B. Experimental Investigation on Stress Concentration Factors of Cold-formed High Strength Steel Tubular X-Joints, Engineering Structures 2021;243:112408.

[5] Pandey M and Young B. Post-Fire Behaviour of Cold-Formed High Strength Steel Tubular T- and X-Joints, Journal of Constructional Steel Research 2021;186:106859.

[6] Pandey M and Young B. Structural performance of cold-formed high strength steel tubular X-Joints under brace axial compression. Engineering Structures, 2020; 208:109768.

[7] Pandey M and Young B. Static resistances of cold-formed high strength steel tubular non-90° X-Joints. Engineering Structures 2021;239:112064.

[8] Ono, T., Iwata, M. and Ishida, K. An experimental study on joints of new truss system using rectangular hollow sections. In Tubular Structures. 4th International Symposium, 344-353, 1991.

[9] Davies, G., Owen, J.S., Kelly, R.B. Bird Beak T-Joints in Square Hollow Sections – A Finite Element Investigation. In Proceedings of the sixth International Offshore and Polar Engineering Conference, Los Angeles, U.S.A., Vol. IV, 22-27, 1996.

[10] Davies, G. and Kelly, R.B. Bird Beak Joints in Square Hollow Sections – A Finite Element Investigation. In Proceedings of the fourth Pacific Structural Steel Conference, Singapore, 65-72, 1995.

[11] Owen, J.S., Davies, G., and Kelly, R.B. The influence of member orientation on the resistance of cross joints in square RHS construction." J Constr Steel Res 57(3), 253-278, 2001.

[12] Chen Y and Wang J. Axial compression physical testing of traditional and bird beak SHS T-joints. Journal of Central South University, 22(6), 2015, 2328-2338.

[13] Chen Y and Wang J. Numerical study and design equations of square and diamond bird-beak SHS T-joints under axial compression. Thin-Walled Structures, 97, 2015, 215-224.

[14] Peña A and Chacon R. Structural analysis of diamond bird-beak joints subjected to compressive and tensile forces. Journal of Constructional Steel Research, 2014;98:158-166.

[15] Tong L, Xu G, Yan D and Zhao XL. Fatigue tests and design of diamond bird-beak SHS T-joints under axial loading in brace. Journal of Constructional Steel Research, 2016;118:49-59.

[16] Abaqus/Standard. Version 6.17. USA: K. a. S. Hibbit; 2017.

[17] Pandey M and Young B. Tests of cold-formed high strength steel tubular T-joints. Thin-Walled Struct 2019;143:106200.

[18] Pandey M and Young B. Compression capacities of cold-formed high strength steel tubular T-joints. J Constr Steel Res, 162, 2019:105650.

[19] Pandey M, Chung KF and Young B. Design of cold-formed high strength steel tubular T-joints under compression loads. Thin-Walled Structures 2021;164:107573.

[20] Pandey M, Chung KF and Young B. Numerical investigation and design of fully chord supported tubular T-joints. Engineering Structures 2021;239:112063.

[21] Ma JL, Chan TM and Young B. Design of cold-formed high strength steel tubular beams. Engineering Structures, 151, 2017, pp.432-443.

[22] Ma JL, Chan TM and Young B. Cold-formed high strength steel tubular beam-columns. Engineering Structures, 230, 2021, p.111618.

[23] Crockett P. Finite element analysis of welded tubular connections. PhD Thesis, University of Nottingham, 1994.
[24] AWS D1.1/D1.1M, Structural Welding Code – Steel, American Welding Society (AWS), Miami, USA, 2020.
[25] Li HT and Young B. Cold-formed high-strength steel tubular structural members under combined bending and bearing. ASCE Journal of Structural Engineering, 2019, 145(8): 04019081.
[26] Li HT and Young B. Cold-formed stainless steel RHS members undergoing combined bending and web crippling: Testing, modelling and design. Engineering Structures, 250, 2022, 113466.
[27] Li QY and Young B. Design of cold-formed steel built-up open section members under combined compression and bending. Thin-Walled Structures. 2022; 172:108890.
[28] Li QY and Young B. Experimental and numerical investigation on cold-formed steel built-up section pin-ended columns. Thin-Walled Structures. 2022; 170:108444.
[29] ANSI/AISC 360. Specification for Structural Steel Buildings. American Institution of Steel Construction, Chicago, USA; 2016.
[30] BS ISO 14346. Static design procedure for welded hollow-section joints – Recommendations. British Standard International Standards, Geneva, Switzerland; 2013.
[31] IIW Doc. XV-1402-12 and IIW Doc. XV-E-12-433. Static design procedure for welded hollow section joints – Recommendations. International Institute of Welding, Paris, France, 2012.
[32] Packer JA, Wardenier J, Zhao XL, Vegte GJ van der, Kurobane Y. Design guide for rectangular hollow section (RHS) joints under predominantly static loading. Comite´ International pour le Developpement et l'Etude de la Construction TuECbulaire (CIDECT), Design Guide No. 3, 2nd edn., LSS Verlag, Dortmund, Germany, 2009.
[33] Eurocode 3 (EC3), Design of Steel Structures-Part 1-8: Design of Joints, prEN 1993-1-8, European Committee for Standardization, CEN, Brussels, Belgium, 2021.
[34] Stroetmann R, Kastner T, Halsig A and Mayr P. Mechanical properties and a new design approach for welded joints at high strength steels. Hong Kong:Engineering Research and Practice for Steel Construction; 2018:79–90.
[35] Javidan F, Heidarpour A, Zhao XL, Hutchinson CR and Minkkinen J. Effect of weld on the mechanical properties of high strength and ultra-high strength steel tubes in fabricated hybrid sections. Eng Struct 2016;118:16–27.
[36] Amraei M., Ahola A., Afkhami S., Bjork T., Heidarpour A. and Zhao X.L. .Effects of heat input on the mechanical properties of butt-welded high and ultra-high strength steels, Engineering Structures, 2019, 198, 109460.
[37] Amraei M., Afkhami S., Javaheri V., Larkiola J., Skriko T., Bjork T. and Zhao X.L. .Mechanical properties and microstructural evaluation of the heat-affected zone in ultra-high strength steels, Thin-Walled Structures, 2020, 157, 107072.
[38] SSAB. Strenx Tube 960 MH. Data Sheet 2043, Sweden, 2017.
[39] EN 10219-2. Cold formed welded structural hollow sections of non-alloy and fine grain steels-Part 2: Tolerances, dimensions and sectional properties. European Committee for Standardization (CEN), Brussels, Belgium; 2006.
[40] AISI S100. North American Specification for the design of cold-formed steel structural members. American Iron and Steel Institute (AISI), Washington, D.C., USA, 2016.
[41] EN 1990. Eurocode: Basis of structural design. European Committee for Standardization (CEN), Brussels, Belgium, 2002.
[42] ASCE/SEI 7. Minimum Design Loads for Buildings and Other Structures. American Society of Civil Engineers (ASCE), New York, USA, 2016.

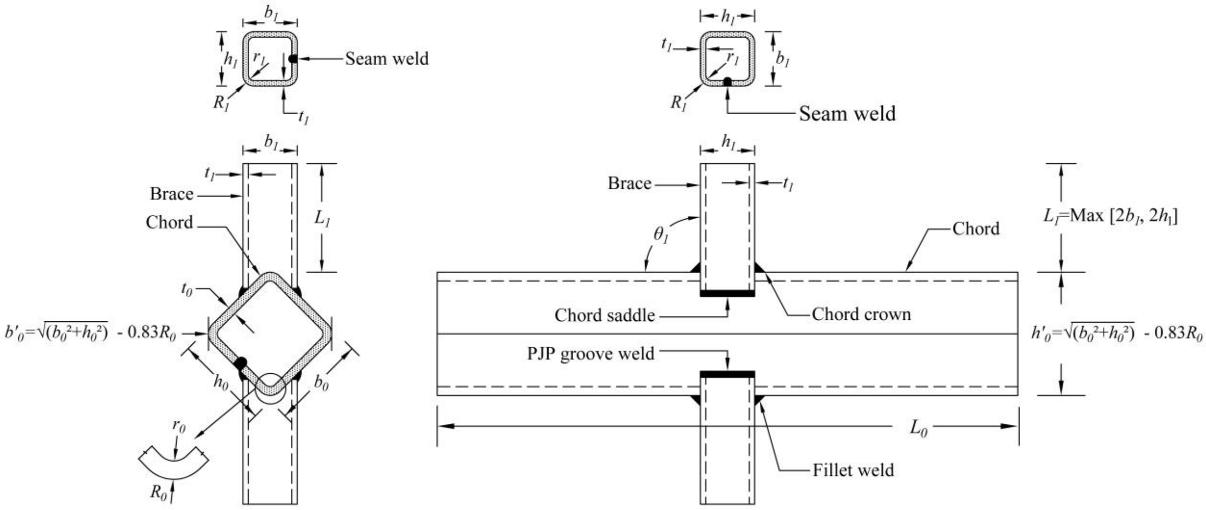

Fig. 1. Definitions of notations for SBB X-joint (also valid for SBB T-joint).

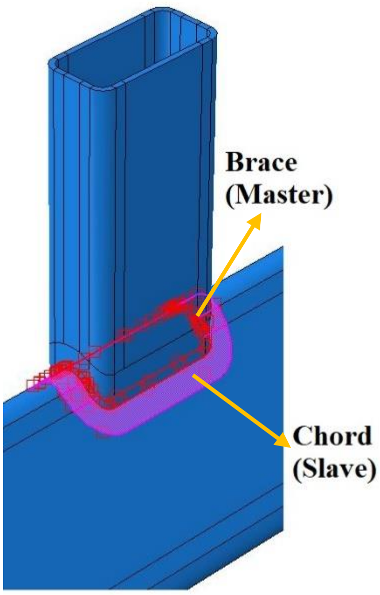

(a) Brace-to-Chord contact interaction.

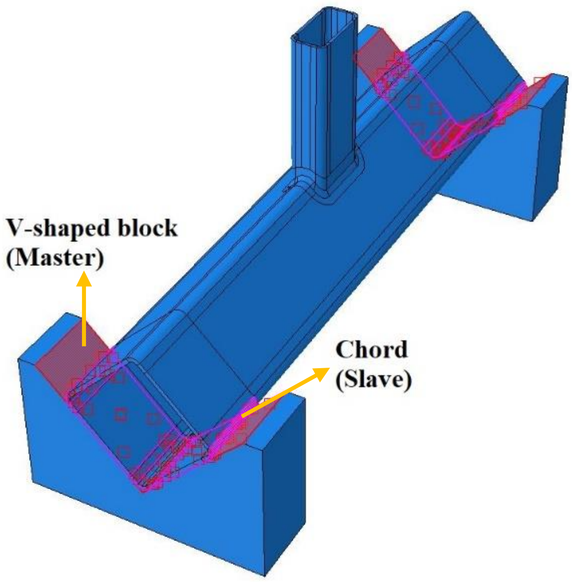

(b) Chord-to-V-shaped block contact interaction.

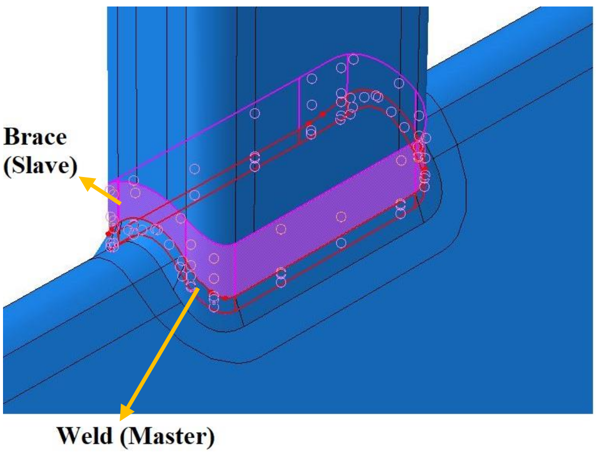

(c) Brace-to-Weld tie connection.

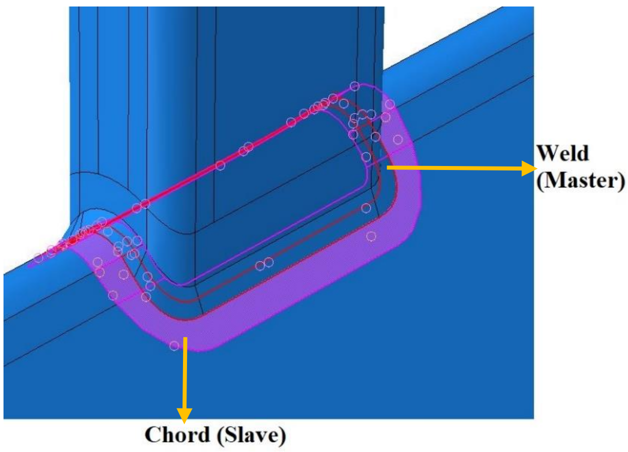

(d) Chord-to-Weld tie connection.

Fig. 2. Typical contact and tie interactions in a SBB FE model.

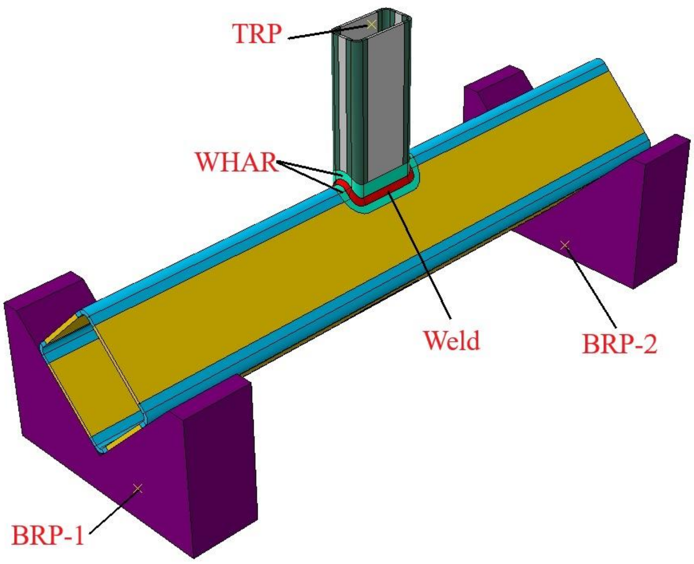

(a) Typical SBB T-joint FE model.

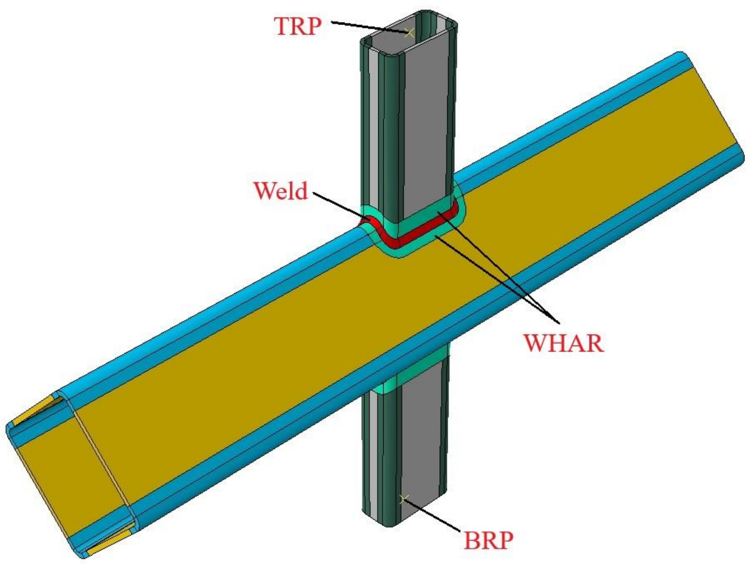

(b) Typical SBB X-joint FE model.

Fig. 3. Typical FE models of SBB T- and X-joints.

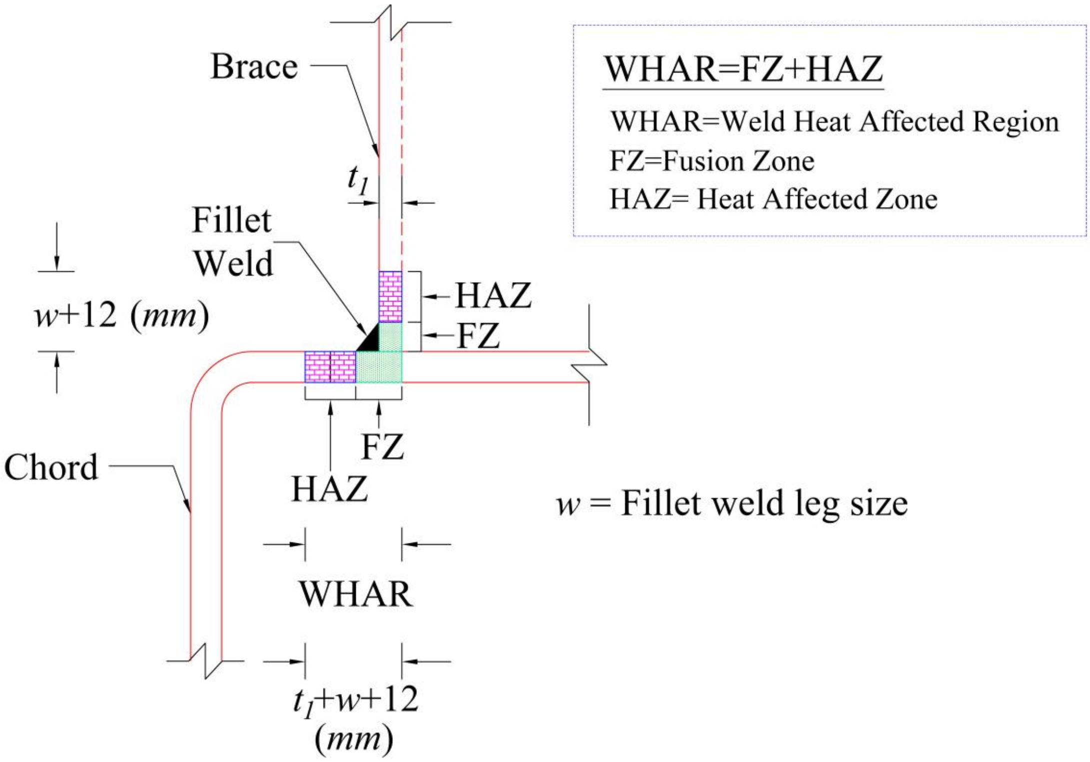

Fig. 4. Definition of weld heat affected region (WHAR) [19].

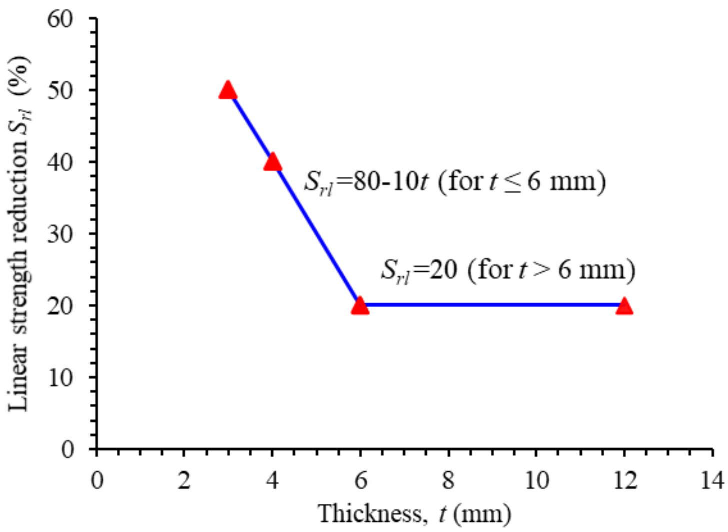

Fig. 5. Linear strength reduction model for WHAR of S900 and S960 steel grades tubular joints [19].

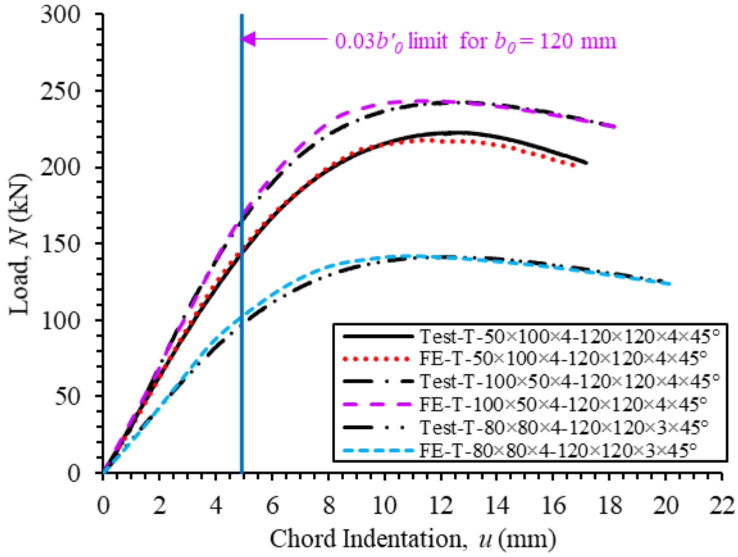

Fig. 6. Test vs FE load-chord indentation curves for SBB T-joints.

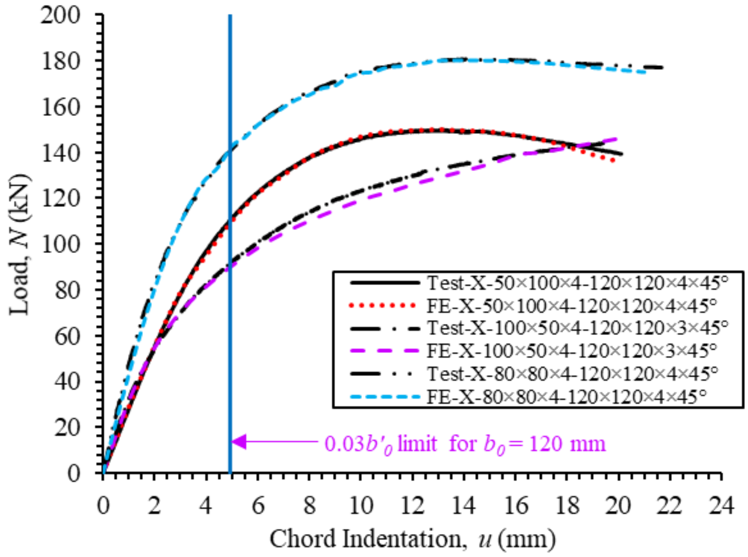

Fig. 7. Test vs FE load-chord indentation curves for SBB X-joints.

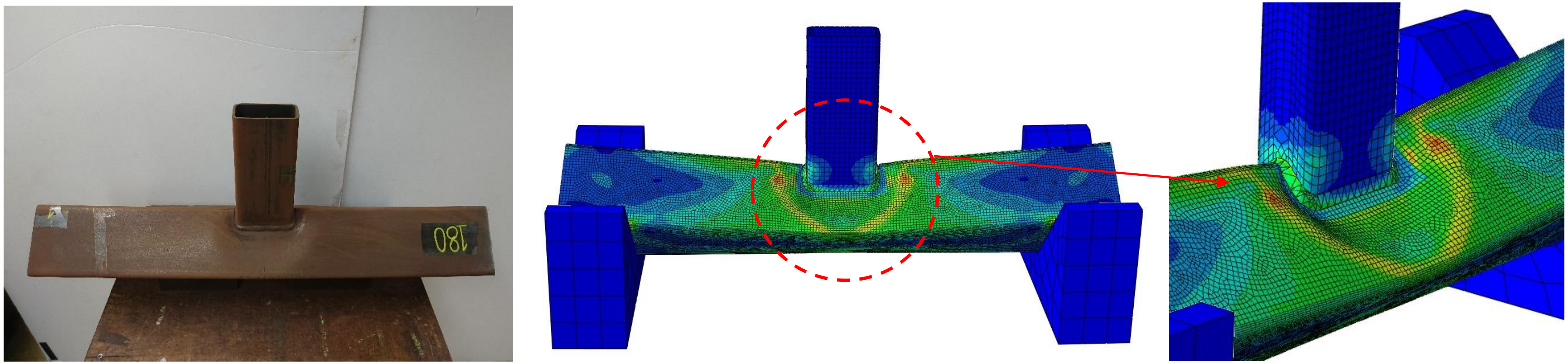

(a) Test vs FE comparison for chord crown failure (C) mode of SBB T-joint (T-50×100×4-120×120×3×45°).

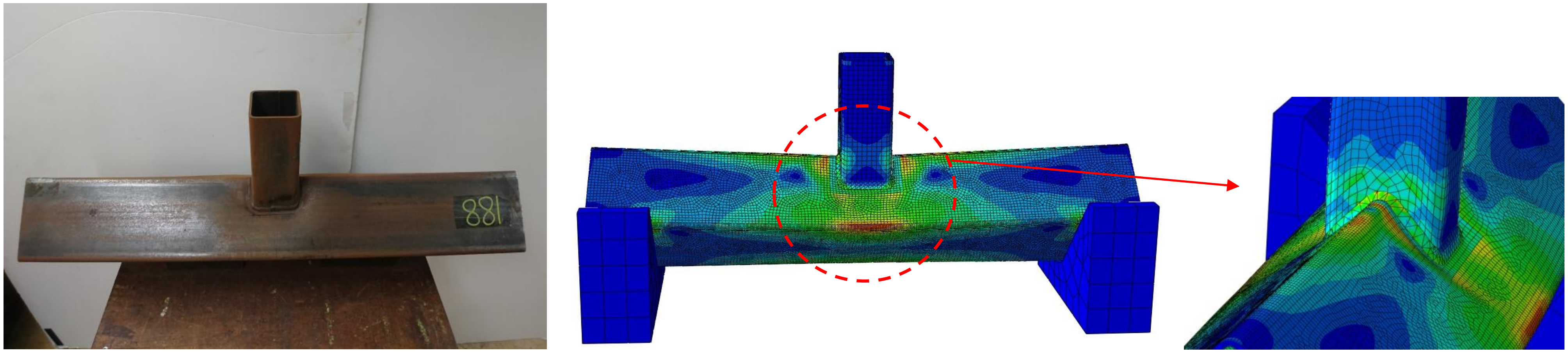

(b) Test vs FE comparison for chord crown failure (C) mode of SBB T-joint (T-80×80×4-140×140×4×45°).

Fig. 8. Test vs FE failure mode comparisons for SBB T-joints.

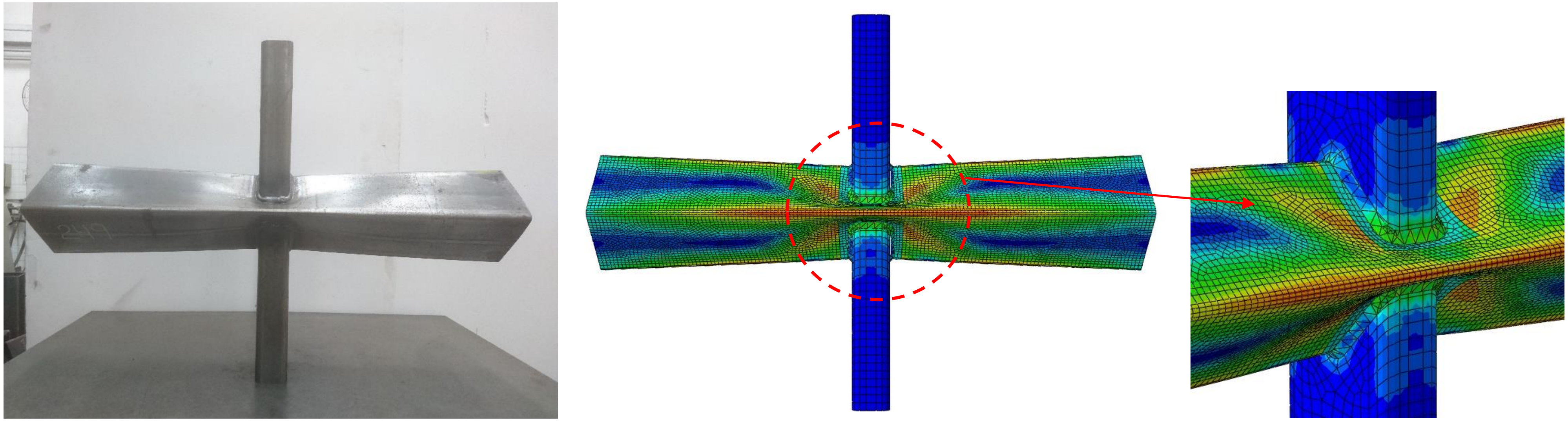

(a) Test vs FE comparison for chord crown failure (C) mode of SBB X-joint (X-100×50×4-120×120×3×45°).

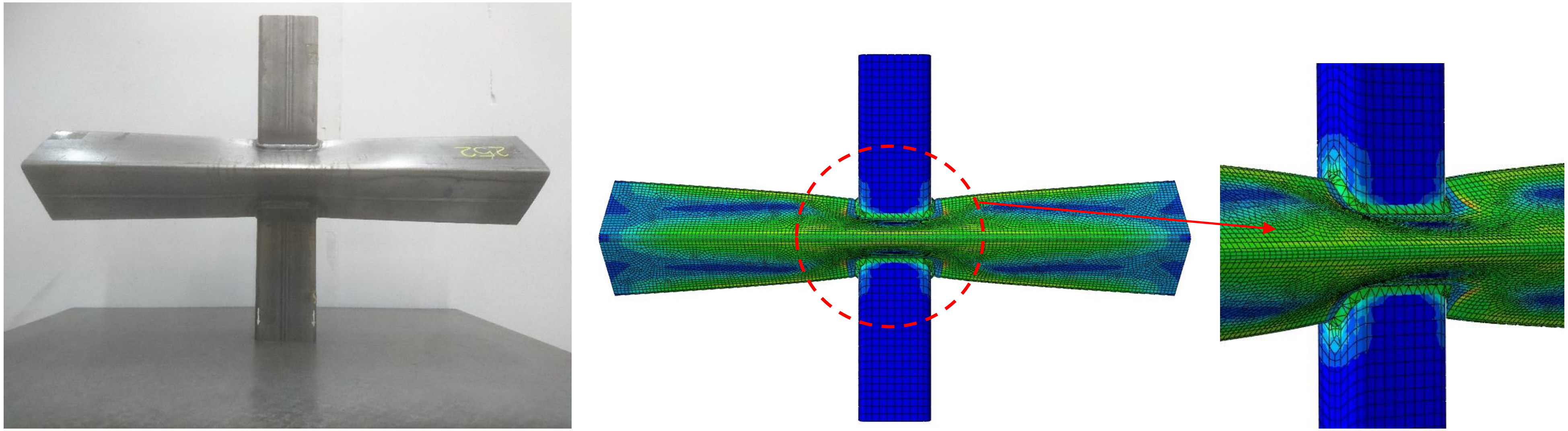

(b) Test vs FE comparison for chord crown failure (C) mode of SBB X-joint (X-50×100×4-120×120×3×45°).

Fig. 9. Test vs FE failure mode comparisons for SBB X-joints.

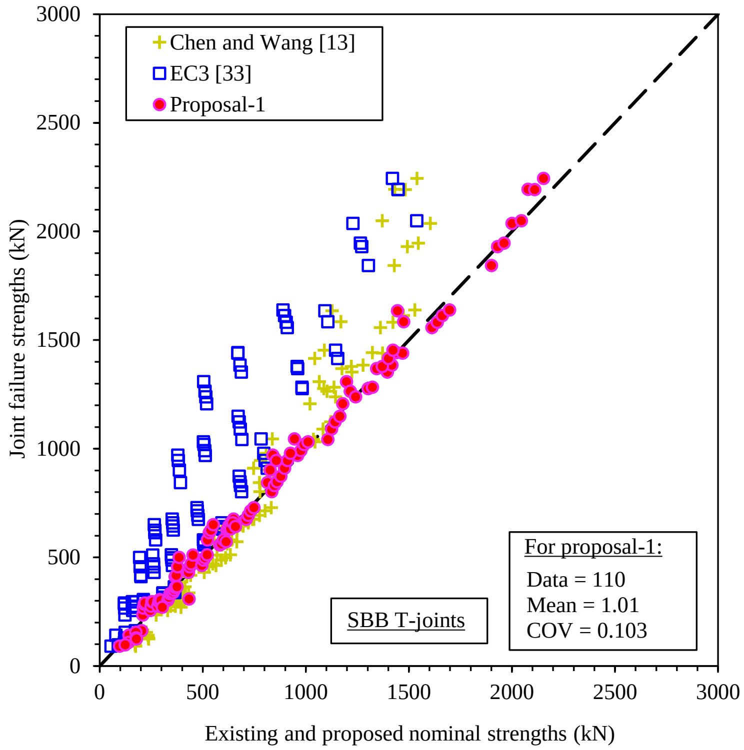

(a) Comparisons of test and FE joint failure strengths ($N_{f,T}$) with existing and proposed nominal strengths for SBB T-joints failed by chord crown failure (C) mode.

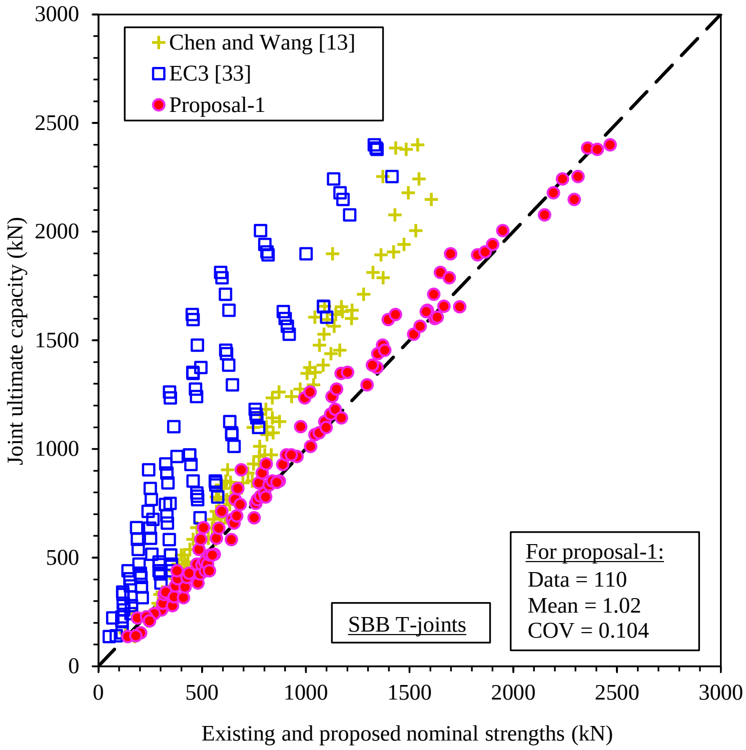

(b) Comparisons of test and FE ultimate capacities ($N_{max,T}$) with existing and proposed nominal strengths for SBB T-joints failed by chord crown failure (C) mode.

Fig. 10. Comparisons of test and FE strengths with existing and proposed nominal strengths for SBB T-joints.

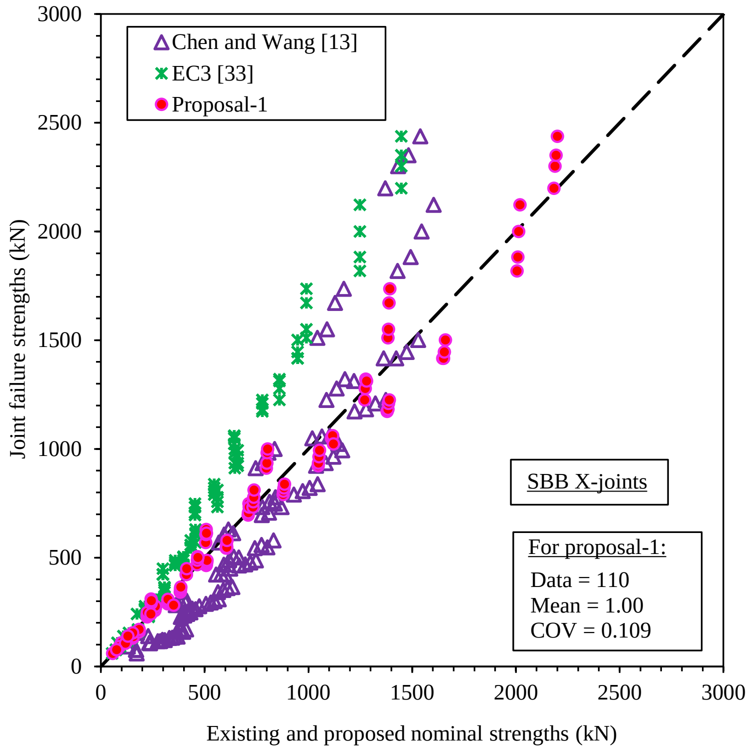

(a) Comparisons of test and FE joint failure strengths ($N_{f,X}$) with existing and proposed nominal strengths for SBB X-joints failed by chord crown failure (C) mode.

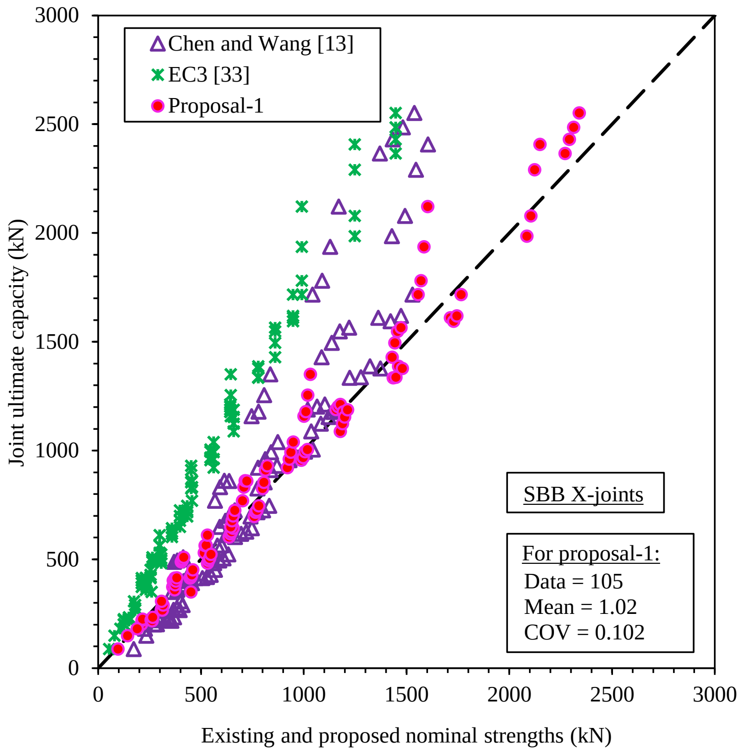

(b) Comparisons of test and FE ultimate capacities ($N_{max,X}$) with existing and proposed nominal strengths for SBB X-joints failed by chord crown failure (C) mode.

Fig. 11. Comparisons of test and FE strengths with existing and proposed nominal strengths for SBB X-joints.

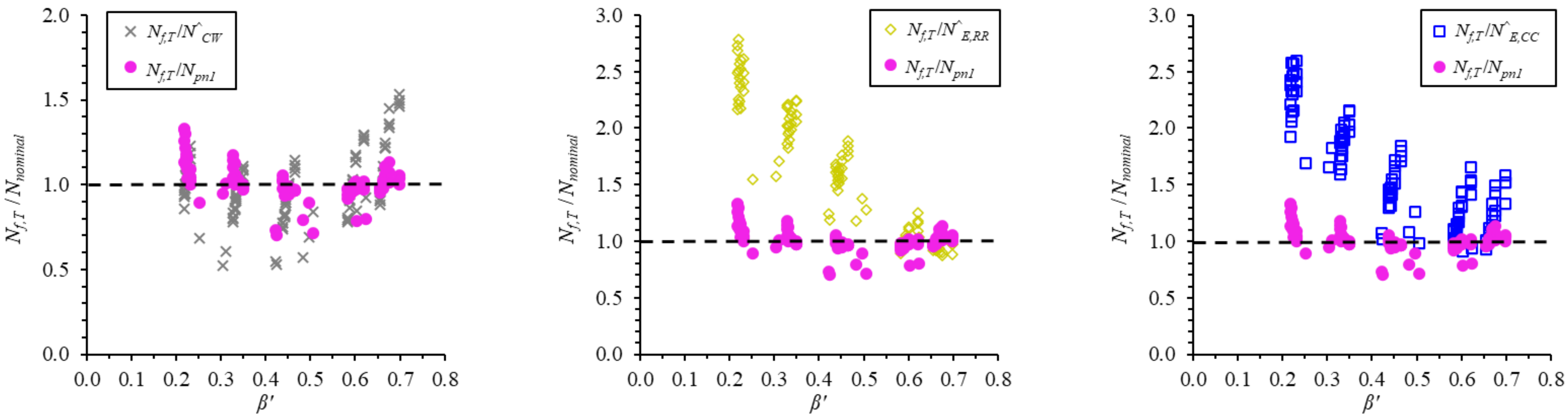

(a) For Chen and Wang [13] (b) For RHS-to-RHS T-joint of EC3 [33] (c) For CHS-to-CHS T-joint of EC3 [33]

Fig. 12. Distributions of joint failure strength ($N_{f,T}$) comparisons ratios for SBB T-joints.

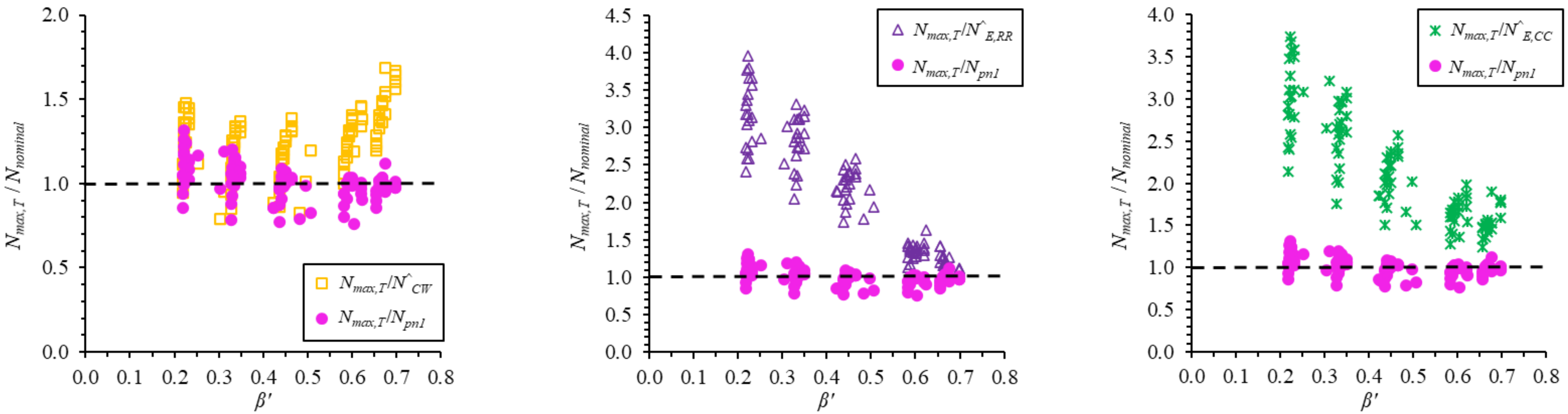

(a) For Chen and Wang [13] (b) For RHS-to-RHS T-joint of EC3 [33] (c) For CHS-to-CHS T-joint of EC3 [33]

Fig. 13. Distributions of joint ultimate capacity ($N_{max,T}$) comparisons ratios for SBB T-joints.

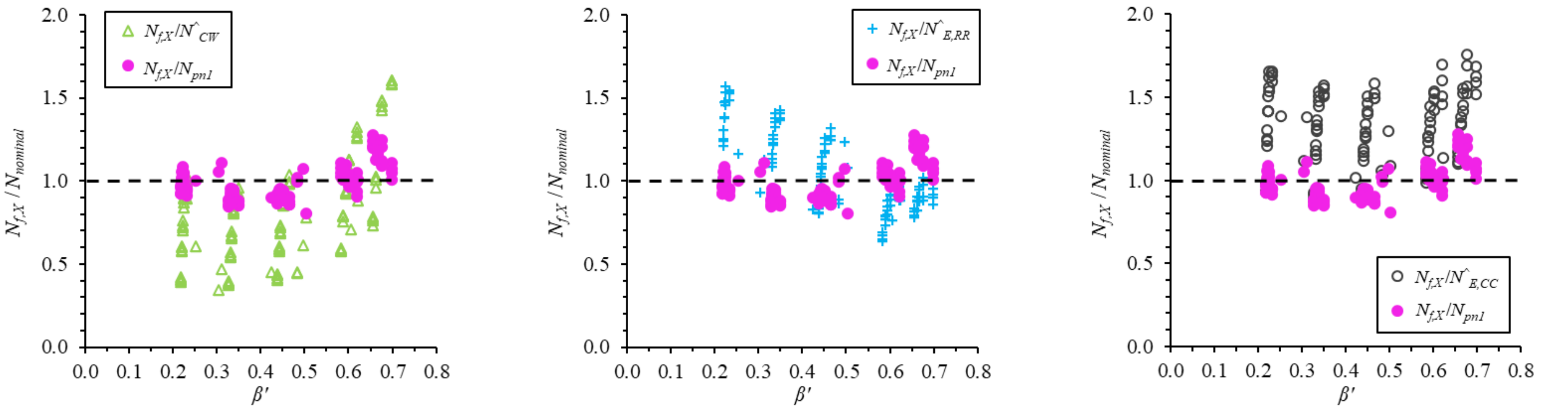

(a) For Chen and Wang [13]
(b) For RHS-to-RHS X-joint of EC3 [33]
(c) For CHS-to-CHS X-joint of EC3 [33]

Fig. 14. Distributions of joint failure strength ($N_{f,X}$) comparisons ratios for SBB X-joints.

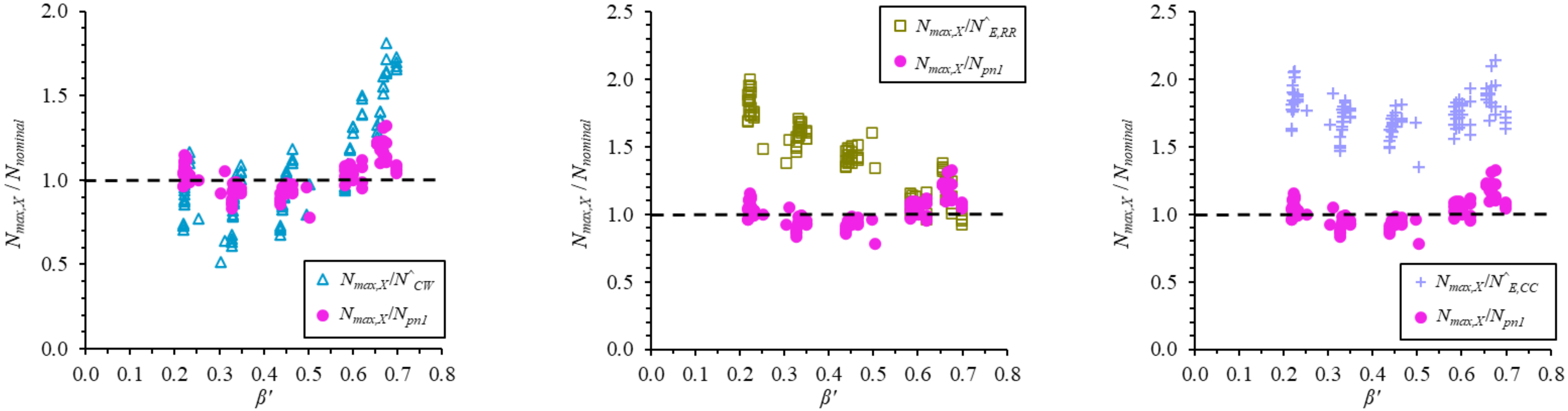

(a) For Chen and Wang [13]
(b) For RHS-to-RHS X-joint of EC3 [33]
(c) For CHS-to-CHS X-joint of EC3 [33]

Fig. 15. Distributions of joint ultimate capacity ($N_{max,X}$) comparisons ratios for SBB X-joints.

Table 1. Test vs FE strength comparisons for SBB T-joints.

Specimens	β'	Test Joint Failure Strengths[#] (kN)	Test Joint Ultimate Capacities[#] (kN)	Numerical Joint Failure Strengths (kN)	Numerical Joint Ultimate Capacities (kN)	Comparisons	
T-b_1×h_1×t_1-b_0×h_0×t_0×ω	$\frac{b_1}{b_0'}$	$N_{f,T}$	$N_{\max,T}$	$N_{f,FE}$	$N_{\max,FE}$	$\frac{N_{f,T}}{N_{f,FE}}$	$\frac{N_{\max,T}}{N_{\max,FE}}$
T-50×100×4-150×150×6×45°	0.25	271.0	440.5	286.1	442.0	0.95	1.00
T-100×50×4-150×150×6×45°	0.51	309.0	440.4	317.8	436.5	0.97	1.01
T-50×100×4-120×120×4×45°	0.31	142.0	222.9	144.5	218.0	0.98	1.02
T-100×50×4-120×120×4×45°	0.62	162.6	242.5	164.9	243.3	0.99	1.00
T-50×100×4-120×120×3×45°	0.30	91.5	137.3	92.2	135.0	0.99	1.02
T-100×50×4-120×120×3×45°	0.60	109.3	154.0	111.9	150.50	0.98	1.02
T-80×80×4-120×120×4×45°	0.50	156.0	228.2	156.1	227.70	1.00	1.00
T-80×80×4-140×140×4×45°	0.42	129.5	209.8	143.8	208.6	0.90	1.01
T-80×80×4-140×140×4×45°-R	0.42	124.8	209.9	125.0	208.6	1.00	1.01
T-80×80×4-120×120×3×45°	0.48	97.9	141.5	102.2	141.9	0.96	1.00
					Mean (P_m)	0.97	1.01
					COV (V_p)	0.031	0.010

Note: [#] Data obtained from Pandey and Young [1].

Table 2. Test vs FE strength comparisons for SBB X-joints.

Specimens	β'	Test Joint Failure Strengths[#] (kN)	Test Joint Ultimate Capacities[#] (kN)	Numerical Joint Failure Strengths (kN)	Numerical Joint Ultimate Capacities (kN)	Comparisons	
X-b_1×h_1×t_1-b_0×h_0×t_0×ω	$\frac{b_1}{b_0'}$	$N_{f,X}$	$N_{\max,X}$	$N_{f,FE}$	$N_{\max,FE}$	$\frac{N_{f,X}}{N_{f,FE}}$	$\frac{N_{\max,X}}{N_{\max,FE}}$
X-50×100×4-150×150×6×45°	0.25	241.2	307.2	240.3	310.0	1.00	0.99
X-100×50×4-150×150×6×45°	0.50	281.7	350.1	282.0	346.1	1.00	1.01
X-50×100×4-120×120×4×45°	0.31	109.2	149.9	108.4	150.2	1.01	1.00
X-100×50×4-120×120×4×45°	0.62	153.6	-	154.8	-	0.99	-
X-50×100×4-120×120×3×45°	0.30	59.6	88.7	60.6	90.7	0.98	0.98
X-100×50×4-120×120×3×45°	0.61	92.0	-	90.1	-	1.02	-
X-80×80×4-120×120×4×45°	0.50	139.7	180.8	140.1	180.1	1.00	1.00
X-80×80×4-140×140×4×45°	0.42	106.5	-	110.6	-	0.96	-
X-80×80×4-120×120×3×45°	0.48	75.4	-	77.9	-	0.97	-
X-80×80×4-120×120×3×45°-R	0.48	76.6	-	78.1	-	0.98	-
					Mean (P_m)	0.99	1.00
					COV (V_p)	0.018	0.013

Note: " - " denotes not applicable; [#] Data obtained from Pandey and Young [2].

Table 3. Ranges of critical parameters used in parametric study.

Parameters	Validity Ranges
β (b_1/b_0)	[0.30 to 0.90]
β' (b_1/b_0')	[0.22 to 0.70]
2γ (b_0/t_0)	[16.6 to 40]
τ (t_1/t_0)	[0.50 to 1.28]

Table 4. Mechanical properties of tubular member and weld adopted in parametric study.

Materials	Measured Mechanical Properties						
	E (GPa)	$\sigma_{0.2}$ (MPa)	$\varepsilon_{0.2}$ (%)	σ_u (MPa)	ε_u (%)	ε_f (%)	n
SHS/RHS (150×150×6) [17]	208.5	1059.1	0.71	1145.7	1.48	9.37[#]	5.31
Weld Material [18]	202.7	965.2	0.68	1023.4	5.41	17.15[*]	8.13

Note: [#]fracture strain based on 50 mm gauge length; [*]fracture strain based on 25 mm gauge length.

Table 5. Comparisons between test and FE strengths with existing and proposed nominal strengths for SBB T-joints failed by chord crown failure (C) mode.

Specimens	β'	Joint Failure Strengths (kN)	Joint Ultimate Capacities (kN)	Comparisons for Joint Failure Strengths						Comparisons for Joint Ultimate Capacities					
T-b_1×h_1×t_1-b_0×h_0×t_0×ω	$\frac{b_1}{b_0^1}$	$N_{f,T}$	$N_{\max,T}$	$\frac{N_{f,T}}{\hat{N}_{CW}}$	$\frac{N_{f,T}}{\hat{N}_{E,RR}}$	$\frac{N_{f,T}}{\hat{N}_{E,CC}}$	$\frac{N_{f,T}}{N_{pn1}}$	$\frac{N_{f,T}}{N_{pn2}}$	$\frac{N_{f,T}}{N_{pn3}}$	$\frac{N_{\max,T}}{\hat{N}_{CW}}$	$\frac{N_{\max,T}}{\hat{N}_{E,RR}}$	$\frac{N_{\max,T}}{\hat{N}_{E,CC}}$	$\frac{N_{\max,T}}{N_{pn1}}$	$\frac{N_{\max,T}}{N_{pn2}}$	$\frac{N_{\max,T}}{N_{pn3}}$
T-60×60×6-200×200×12×45°	0.23	1207.6	1375.8	1.18	2.33	2.33	1.02	0.94	1.00	1.35	2.81	2.79	1.02	0.95	0.93
T-60×60×7.8-200×200×12×45°	0.23	1308.9	1478.6	1.23	2.61	2.60	1.09	1.02	1.09	1.39	3.14	3.10	1.08	1.02	0.99
T-60×60×9.6-200×200×12×45°	0.23	1265.4	1596.1	1.15	2.49	2.48	1.04	0.98	1.05	1.45	3.57	3.50	1.14	1.10	1.07
T-60×60×12-200×200×12×45°	0.23	1238.8	1619.2	1.08	2.41	2.41	1.00	0.96	1.03	1.42	3.66	3.58	1.13	1.11	1.09
T-90×90×6-200×200×12×45°	0.35	1353.8	1638.9	1.11	2.06	1.97	0.97	1.01	0.97	1.34	2.72	2.61	1.03	0.97	0.94
T-90×90×7.8-200×200×12×45°	0.35	1384.8	1712.3	1.08	2.12	2.03	0.98	1.04	1.00	1.34	2.93	2.80	1.06	1.01	0.98
T-90×90×9.6-200×200×12×45°	0.35	1443.0	1813.5	1.09	2.25	2.15	1.00	1.08	1.04	1.37	3.23	3.08	1.10	1.07	1.04
T-90×90×12-200×200×12×45°	0.35	1440.1	1788.0	1.05	2.24	2.15	0.98	1.08	1.04	1.30	3.15	3.01	1.06	1.06	1.03
T-120×120×6-200×200×12×45°	0.47	1558.0	1893.6	1.14	1.75	1.71	0.97	1.10	0.98	1.39	2.35	2.32	1.04	0.99	0.94
T-120×120×7.8-200×200×12×45°	0.47	1582.9	1907.8	1.11	1.79	1.75	0.97	1.12	1.00	1.34	2.38	2.35	1.02	0.99	0.95
T-120×120×9.6-200×200×12×45°	0.47	1613.7	1941.1	1.10	1.84	1.80	0.97	1.14	1.02	1.32	2.45	2.42	1.02	1.01	0.96
T-120×120×12-200×200×12×45°	0.47	1639.3	2005.5	1.07	1.88	1.84	0.97	1.16	1.03	1.31	2.59	2.57	1.03	1.05	0.99
T-160×160×6-200×200×12×45°	0.62	1843.5	2077.6	1.29	1.09	1.41	0.97	1.08	1.05	1.45	1.29	1.72	0.97	0.91	0.90
T-160×160×7.8-200×200×12×45°	0.62	1930.6	2179.8	1.29	1.16	1.52	1.00	1.13	1.10	1.46	1.39	1.87	0.99	0.96	0.95
T-160×160×9.6-200×200×12×45°	0.62	1946.2	2243.0	1.26	1.18	1.54	0.99	1.14	1.11	1.45	1.46	1.98	1.00	0.99	0.97
T-160×160×12-200×200×12×45°	0.62	2036.8	2148.6	1.27	1.25	1.66	1.02	1.19	1.16	1.34	1.36	1.82	0.94	0.95	0.93

T-180×180×6-200×200×12×45°	0.70	2050.0	2254.6	1.50	0.88	1.33	1.00	0.89	1.17	1.64	1.02	1.59	0.98	0.84	0.96
T-180×180×7.8-200×200×12×45°	0.70	2194.2	2384.9	1.53	0.98	1.52	1.06	0.95	1.26	1.67	1.11	1.78	1.01	0.89	1.01
T-180×180×9.6-200×200×12×45°	0.70	2193.5	2378.9	1.48	0.98	1.52	1.04	0.95	1.26	1.60	1.10	1.77	0.99	0.89	1.01
T-180×180×12-200×200×12×45°	0.70	2244.8	2399.5	1.46	1.01	1.58	1.04	0.97	1.29	1.56	1.12	1.80	0.97	0.90	1.02
T-60×60×5-200×200×10×45°	0.23	844.6	965.4	1.09	2.17	2.15	1.04	0.93	0.98	1.25	2.59	2.55	1.01	0.95	0.91
T-60×60×6.5-200×200×10×45°	0.23	902.4	1102.6	1.11	2.37	2.34	1.09	1.00	1.05	1.36	3.10	3.04	1.13	1.09	1.04
T-60×60×8-200×200×10×45°	0.23	970.8	1236.0	1.16	2.60	2.57	1.16	1.07	1.13	1.47	3.67	3.57	1.24	1.22	1.16
T-60×60×10-200×200×10×45°	0.23	946.8	1262.8	1.09	2.52	2.49	1.11	1.05	1.10	1.45	3.79	3.69	1.24	1.25	1.19
T-90×90×5-200×200×10×45°	0.34	970.1	1241.2	1.04	1.99	1.90	1.01	1.03	0.98	1.33	2.75	2.62	1.10	1.05	1.01
T-90×90×6.5-200×200×10×45°	0.34	992.0	1275.8	1.02	2.04	1.95	1.02	1.05	1.01	1.31	2.86	2.73	1.11	1.08	1.03
T-90×90×8-200×200×10×45°	0.34	1019.7	1348.8	1.01	2.12	2.02	1.03	1.08	1.03	1.34	3.11	2.96	1.15	1.14	1.09
T-90×90×10-200×200×10×45°	0.34	1032.0	1353.3	0.99	2.15	2.05	1.02	1.09	1.05	1.30	3.12	2.97	1.13	1.14	1.10
T-120×120×5-200×200×10×45°	0.45	1043.0	1295.2	1.01	1.56	1.51	0.94	1.03	0.93	1.25	2.06	2.01	1.00	0.95	0.91
T-120×120×6.5-200×200×10×45°	0.45	1091.6	1386.6	1.01	1.65	1.60	0.97	1.08	0.97	1.28	2.26	2.21	1.05	1.02	0.97
T-120×120×8-200×200×10×45°	0.45	1123.7	1438.9	1.00	1.71	1.66	0.98	1.11	1.00	1.28	2.38	2.33	1.07	1.05	1.01
T-120×120×10-200×200×10×45°	0.45	1150.3	1455.1	0.99	1.76	1.71	0.99	1.13	1.02	1.25	2.42	2.37	1.05	1.07	1.02
T-160×160×5-200×200×10×45°	0.60	1277.3	1529.1	1.18	1.02	1.30	0.98	1.01	1.02	1.41	1.28	1.66	1.01	0.90	0.93
T-160×160×6.5-200×200×10×45°	0.60	1283.9	1564.8	1.13	1.03	1.31	0.97	1.02	1.02	1.38	1.32	1.72	1.01	0.92	0.95
T-160×160×8-200×200×10×45°	0.60	1369.3	1632.8	1.16	1.11	1.43	1.02	1.09	1.09	1.39	1.39	1.83	1.03	0.96	1.00
T-160×160×10-200×200×10×45°	0.60	1379.5	1600.8	1.13	1.12	1.44	1.01	1.10	1.10	1.31	1.36	1.78	0.99	0.94	0.98
T-180×180×5-200×200×10×45°	0.68	1415.9	1607.3	1.36	0.87	1.23	1.01	0.81	1.12	1.54	1.02	1.46	0.98	0.75	0.95
T-180×180×6.5-200×200×10×45°	0.68	1453.5	1657.7	1.33	0.90	1.27	1.02	0.83	1.15	1.52	1.06	1.53	1.00	0.77	0.98
T-180×180×8-200×200×10×45°	0.68	1634.7	1898.7	1.45	1.04	1.50	1.13	0.93	1.29	1.68	1.26	1.90	1.12	0.88	1.12
T-180×180×10-200×200×10×45°	0.68	1584.9	1654.3	1.35	1.00	1.43	1.08	0.90	1.25	1.41	1.05	1.52	0.95	0.77	0.98
T-60×60×4-200×200×8×45°	0.22	580.7	677.2	1.05	2.24	2.15	1.11	1.00	1.01	1.22	2.70	2.58	1.05	1.05	0.96
T-60×60×5.2-200×200×8×45°	0.22	614.7	768.5	1.06	2.40	2.30	1.16	1.06	1.07	1.33	3.18	3.02	1.17	1.19	1.09
T-60×60×6.4-200×200×8×45°	0.22	624.6	818.5	1.04	2.45	2.34	1.16	1.08	1.09	1.36	3.45	3.27	1.22	1.26	1.16
T-60×60×8-200×200×8×45°	0.22	651.0	904.5	1.05	2.57	2.46	1.18	1.12	1.14	1.45	3.96	3.74	1.31	1.40	1.28
T-90×90×4-200×200×8×45°	0.33	626.5	750.0	0.94	1.90	1.76	1.02	1.03	0.95	1.13	2.36	2.18	0.99	0.99	0.91
T-90×90×5.2-200×200×8×45°	0.33	644.7	843.9	0.93	1.96	1.82	1.03	1.06	0.98	1.21	2.73	2.52	1.09	1.11	1.03
T-90×90×6.4-200×200×8×45°	0.33	659.7	889.4	0.92	2.02	1.87	1.04	1.08	1.00	1.24	2.93	2.70	1.13	1.17	1.08
T-90×90×8-200×200×8×45°	0.33	677.2	931.2	0.91	2.08	1.92	1.04	1.11	1.03	1.25	3.11	2.87	1.15	1.23	1.13
T-120×120×4-200×200×8×45°	0.45	675.3	853.2	0.91	1.51	1.41	0.95	1.03	0.90	1.15	1.99	1.87	0.98	0.97	0.90
T-120×120×5.2-200×200×8×45°	0.45	693.7	928.7	0.90	1.56	1.46	0.96	1.06	0.93	1.20	2.21	2.08	1.05	1.05	0.98
T-120×120×6.4-200×200×8×45°	0.45	714.7	972.8	0.89	1.61	1.51	0.98	1.09	0.95	1.21	2.34	2.21	1.07	1.10	1.02
T-120×120×8-200×200×8×45°	0.45	729.6	973.4	0.88	1.65	1.55	0.98	1.11	0.97	1.17	2.34	2.21	1.05	1.10	1.02
T-160×160×4-200×200×8×45°	0.59	802.7	1012.0	1.03	0.96	1.17	0.96	0.97	0.96	1.30	1.25	1.55	0.99	0.90	0.93

T-160×160×5.2-200×200×8×45°	0.59	831.5	1066.8	1.02	1.00	1.22	0.98	1.01	0.99	1.31	1.34	1.66	1.02	0.95	0.98
T-160×160×6.4-200×200×8×45°	0.59	848.4	1075.6	1.01	1.02	1.25	0.99	1.03	1.01	1.28	1.35	1.68	1.01	0.96	0.98
T-160×160×8-200×200×8×45°	0.59	874.4	1126.1	1.00	1.06	1.29	1.00	1.06	1.05	1.29	1.43	1.78	1.03	1.01	1.03
T-180×180×4-200×200×8×45°	0.67	910.3	1100.0	1.22	0.90	1.12	1.02	0.79	1.08	1.47	1.11	1.42	1.00	0.76	0.97
T-180×180×5.2-200×200×8×45°	0.67	946.5	1160.6	1.21	0.94	1.18	1.04	0.82	1.12	1.49	1.19	1.53	1.04	0.80	1.03
T-180×180×6.4-200×200×8×45°	0.67	980.0	1182.7	1.21	0.98	1.23	1.06	0.85	1.16	1.47	1.21	1.57	1.04	0.82	1.05
T-180×180×8-200×200×8×45°	0.67	1045.8	1143.9	1.25	1.05	1.34	1.11	0.90	1.24	1.37	1.17	1.50	0.98	0.79	1.01
T-60×60×3.33-200×200×6.66×45°	0.22	411.5	470.2	0.98	2.21	2.06	1.13	1.02	1.00	1.11	2.59	2.40	0.99	1.04	0.92
T-60×60×4.33-200×200×6.66×45°	0.22	418.6	537.7	0.95	2.26	2.10	1.13	1.04	1.02	1.22	3.04	2.81	1.11	1.19	1.06
T-60×60×5.33-200×200×6.66×45°	0.22	457.8	584.4	1.00	2.50	2.33	1.22	1.13	1.11	1.28	3.37	3.11	1.18	1.30	1.15
T-60×60×6.66-200×200×6.66×45°	0.22	499.9	638.8	1.06	2.78	2.58	1.30	1.24	1.21	1.35	3.77	3.48	1.26	1.42	1.26
T-90×90×3.33-200×200×6.66×45°	0.33	431.4	516.4	0.85	1.82	1.64	1.00	1.01	0.91	1.02	2.24	2.01	0.93	0.98	0.88
T-90×90×4.33-200×200×6.66×45°	0.33	457.8	589.9	0.87	1.95	1.75	1.05	1.08	0.97	1.12	2.62	2.36	1.04	1.12	1.00
T-90×90×5.33-200×200×6.66×45°	0.33	470.2	635.7	0.86	2.01	1.81	1.06	1.11	1.00	1.16	2.87	2.58	1.10	1.20	1.08
T-90×90×6.66-200×200×6.66×45°	0.33	511.1	713.1	0.90	2.21	1.99	1.13	1.20	1.08	1.25	3.32	2.98	1.20	1.35	1.21
T-120×120×3.33-200×200×6.66×45°	0.44	463.0	583.2	0.82	1.45	1.31	0.94	1.01	0.86	1.03	1.88	1.71	0.91	0.95	0.86
T-120×120×4.33-200×200×6.66×45°	0.44	488.4	659.4	0.83	1.54	1.40	0.97	1.06	0.91	1.12	2.17	1.98	1.01	1.07	0.97
T-120×120×5.33-200×200×6.66×45°	0.44	498.6	692.4	0.82	1.57	1.43	0.98	1.09	0.93	1.14	2.30	2.10	1.04	1.12	1.02
T-120×120×6.66-200×200×6.66×45°	0.44	512.1	744.8	0.81	1.62	1.47	0.98	1.12	0.95	1.18	2.51	2.30	1.09	1.21	1.09
T-160×160×3.33-200×200×6.66×45°	0.59	557.5	684.1	0.94	0.94	1.10	0.96	0.96	0.93	1.16	1.18	1.40	0.91	0.87	0.87
T-160×160×4.33-200×200×6.66×45°	0.59	562.4	767.5	0.91	0.95	1.11	0.95	0.97	0.94	1.24	1.34	1.60	1.00	0.97	0.98
T-160×160×5.33-200×200×6.66×45°	0.59	580.5	783.7	0.91	0.98	1.15	0.97	1.00	0.97	1.22	1.38	1.65	1.00	0.99	1.00
T-160×160×6.66-200×200×6.66×45°	0.59	572.5	797.6	0.86	0.97	1.14	0.93	0.99	0.95	1.20	1.40	1.68	1.00	1.01	1.02
T-180×180×3.33-200×200×6.66×45°	0.66	630.0	780.0	1.11	0.92	1.06	1.01	0.77	1.03	1.37	1.16	1.36	0.97	0.75	0.96
T-180×180×4.33-200×200×6.66×45°	0.66	631.0	834.6	1.06	0.92	1.06	0.99	0.77	1.03	1.41	1.25	1.48	1.02	0.80	1.03
T-180×180×5.33-200×200×6.66×45°	0.66	659.7	852.6	1.07	0.97	1.11	1.02	0.80	1.08	1.39	1.28	1.51	1.02	0.82	1.05
T-180×180×6.66-200×200×6.66×45°	0.66	642.2	847.1	1.01	0.94	1.08	0.98	0.78	1.05	1.33	1.28	1.50	0.99	0.82	1.04
T-60×60×2.5-200×200×5×45°	0.22	235.9	259.7	0.86	2.17	1.93	1.13	1.03	0.96	0.95	2.41	2.14	0.85	1.03	0.86
T-60×60×3.25-200×200×5×45°	0.22	266.8	290.4	0.93	2.49	2.21	1.26	1.17	1.09	1.01	2.74	2.43	0.94	1.15	0.96
T-60×60×4-200×200×5×45°	0.22	285.7	331.0	0.96	2.69	2.38	1.33	1.25	1.17	1.12	3.18	2.81	1.05	1.31	1.09
T-60×60×5-200×200×5×45°	0.22	290.0	342.0	0.94	2.73	2.42	1.32	1.27	1.19	1.11	3.30	2.92	1.05	1.35	1.13
T-90×90×2.5-200×200×5×45°	0.33	255.6	279.4	0.78	1.86	1.60	1.04	1.06	0.91	0.85	2.06	1.76	0.78	0.94	0.80
T-90×90×3.25-200×200×5×45°	0.33	275.2	319.6	0.80	2.02	1.73	1.11	1.14	0.98	0.93	2.39	2.04	0.88	1.07	0.91
T-90×90×4-200×200×5×45°	0.33	297.3	370.0	0.84	2.20	1.88	1.18	1.24	1.06	1.04	2.82	2.41	1.00	1.24	1.06
T-90×90×5-200×200×5×45°	0.33	295.0	403.3	0.80	2.18	1.87	1.14	1.23	1.05	1.09	3.11	2.66	1.06	1.35	1.15
T-120×120×2.5-200×200×5×45°	0.44	275.8	315.9	0.75	1.50	1.29	0.98	1.06	0.87	0.86	1.73	1.50	0.77	0.91	0.78
T-120×120×3.25-200×200×5×45°	0.44	296.2	365.0	0.77	1.61	1.40	1.03	1.14	0.93	0.95	2.03	1.76	0.87	1.05	0.90

T-120×120×4-200×200×5×45°	0.44	306.9	408.9	0.77	1.68	1.45	1.06	1.18	0.96	1.03	2.31	2.01	0.96	1.17	1.01
T-120×120×5-200×200×5×45°	0.44	302.4	428.5	0.74	1.65	1.43	1.02	1.16	0.95	1.04	2.43	2.12	0.98	1.23	1.06
T-160×160×2.5-200×200×5×45°	0.58	304.0	384.1	0.79	0.89	0.99	0.92	0.91	0.85	1.00	1.14	1.27	0.80	0.85	0.83
T-160×160×3.25-200×200×5×45°	0.58	316.9	425.1	0.79	0.93	1.03	0.94	0.95	0.89	1.06	1.27	1.43	0.87	0.94	0.91
T-160×160×4-200×200×5×45°	0.58	333.9	468.8	0.80	0.98	1.09	0.98	1.00	0.93	1.13	1.42	1.60	0.94	1.03	1.01
T-160×160×5-200×200×5×45°	0.58	337.5	481.0	0.78	0.99	1.10	0.97	1.02	0.94	1.12	1.46	1.65	0.94	1.06	1.03
T-180×180×2.5-200×200×5×45°	0.66	338.7	440.0	0.92	0.92	0.93	0.95	0.71	0.93	1.19	1.21	1.24	0.85	0.73	0.91
T-180×180×3.25-200×200×5×45°	0.66	349.6	471.0	0.91	0.95	0.96	0.97	0.74	0.96	1.22	1.30	1.34	0.90	0.78	0.98
T-180×180×4-200×200×5×45°	0.66	361.3	512.1	0.91	0.98	1.00	0.98	0.76	0.99	1.28	1.42	1.48	0.96	0.85	1.06
T-180×180×5-200×200×5×45°	0.66	365.4	512.3	0.88	0.99	1.01	0.98	0.77	1.01	1.24	1.42	1.48	0.93	0.85	1.06
T-50×100×4-150×150×6×45°	0.25	271.0	440.5	0.69	1.55	1.69	0.89	0.73	0.84	1.12	2.86	3.09	1.16	1.03	1.10
T-50×100×4-150×150×6×45°	0.25	271.0	440.5	0.69	1.55	1.69	0.89	0.73	0.84	1.12	2.86	3.09	1.16	1.03	1.10
T-100×50×4-150×150×6×45°	0.51	309.0*	440.4*	0.84	1.28	0.98	0.71	1.01	0.70	1.20	1.94	1.51	0.82	1.05	0.77
T-50×100×4-120×120×4×45°	0.31	142.0*	222.9*	0.61	1.71	1.82	1.01	0.88	0.96	0.95	3.02	3.21	1.19	1.14	1.21
T-100×50×4-120×120×4×45°	0.62	162.6*	242.5*	0.93	1.03	0.94	0.80	1.16	0.83	1.38	1.64	1.55	0.90	1.30	0.94
T-50×100×4-120×120×3×45°	0.30	91.5*	137.3*	0.53	1.57	1.66	0.95	0.84	0.90	0.79	2.52	2.66	0.97	1.04	1.08
T-100×50×4-120×120×3×45°	0.60	109.3*	154.0*	0.84	0.97	0.91	0.78	1.05	0.80	1.19	1.41	1.36	0.76	1.09	0.86
T-80×80×4-120×120×4×45°	0.50	156.0*	228.2*	0.69	1.37	1.26	0.89	1.06	0.87	1.01	2.17	2.02	0.98	1.13	0.99
T-80×80×4-140×140×4×45°	0.42	129.5*	209.8*	0.55	1.25	1.07	0.73	0.84	0.69	0.89	2.15	1.85	0.85	1.03	0.89
T-80×80×4-140×140×4×45°-R	0.42	124.8*	209.9*	0.53	1.19	1.02	0.70	0.81	0.66	0.89	2.14	1.85	0.85	1.03	0.88
T-80×80×4-120×120×3×45°	0.48	97.9*	141.5*	0.57	1.18	1.09	0.79	0.91	0.77	0.82	1.78	1.66	0.79	0.97	0.87
Mean (P_m)				1.00	1.60	1.61	1.01	1.02	1.01	1.25	2.16	2.18	1.02	1.03	1.00
COV (V_p)				0.206	0.360	0.285	0.103	0.124	0.115	0.149	0.378	0.294	0.104	0.151	0.095
Resistance factor (ϕ)				1.00	1.00	1.00	0.85	0.80	0.80	1.00	1.00	1.00	0.85	0.80	0.85
Reliability index (β_0)				1.56	2.13	2.48	2.53	2.67	2.68	2.51	2.71	3.21	2.53	2.58	2.50

Note: " * " data obtained from Pandey and Young [1].

Table 6. Comparisons between test and FE strengths with existing and proposed nominal strengths for SBB X-joints failed by chord crown failure (C) mode.

Specimens	β'	Joint Failure Strengths (kN)	Joint Ultimate Capacities (kN)	Comparisons for Joint Failure Strengths						Comparisons for Joint Ultimate Capacities					
X-b_1×h_1×t_1-b_0×h_0×t_0×ω	$\frac{b_1}{b_0^{1}}$	$N_{f,X}$	$N_{\max,X}$	$\frac{N_{f,X}}{\hat{N}_{CW}}$	$\frac{N_{f,X}}{\hat{N}_{E,RR}}$	$\frac{N_{f,X}}{\hat{N}_{E,CC}}$	$\frac{N_{f,X}}{N_{pn1}}$	$\frac{N_{f,X}}{N_{pn2}}$	$\frac{N_{f,X}}{N_{pn3}}$	$\frac{N_{\max,X}}{\hat{N}_{CW}}$	$\frac{N_{\max,X}}{\hat{N}_{E,RR}}$	$\frac{N_{\max,X}}{\hat{N}_{E,CC}}$	$\frac{N_{\max,X}}{N_{pn1}}$	$\frac{N_{\max,X}}{N_{pn2}}$	$\frac{N_{\max,X}}{N_{pn3}}$
X-60×60×6-200×200×12×45°	0.23	1048.5	1188.5	1.03	1.52	1.63	0.94	0.99	0.90	1.17	1.73	1.85	1.03	0.97	0.99
X-60×60×7.8-200×200×12×45°	0.23	1057.3	1202.6	0.99	1.54	1.65	0.95	1.00	0.91	1.13	1.75	1.87	1.03	0.98	1.00
X-60×60×9.6-200×200×12×45°	0.23	1061.4	1211.8	0.96	1.54	1.65	0.95	1.00	0.92	1.10	1.76	1.89	1.03	0.99	1.01
X-60×60×12-200×200×12×45°	0.23	1022.6	1177.9	0.89	1.49	1.59	0.91	0.96	0.88	1.03	1.71	1.83	0.99	0.96	0.98
X-90×90×6-200×200×12×45°	0.35	1172.5	1334.2	0.96	1.37	1.51	0.85	0.94	0.88	1.09	1.56	1.71	0.93	0.93	0.96
X-90×90×7.8-200×200×12×45°	0.35	1182.3	1337.5	0.93	1.38	1.52	0.86	0.94	0.88	1.05	1.56	1.72	0.92	0.93	0.96
X-90×90×9.6-200×200×12×45°	0.35	1209.5	1388.0	0.91	1.41	1.55	0.87	0.97	0.90	1.05	1.62	1.78	0.95	0.97	1.00
X-90×90×12-200×200×12×45°	0.35	1225.2	1377.4	0.89	1.43	1.57	0.88	0.98	0.92	1.00	1.61	1.77	0.93	0.96	0.99
X-120×120×6-200×200×12×45°	0.47	1416.3	1610.9	1.04	1.24	1.50	0.86	0.97	0.92	1.18	1.42	1.70	0.94	1.00	1.00
X-120×120×7.8-200×200×12×45°	0.47	1416.5	1594.9	1.00	1.25	1.50	0.86	0.97	0.92	1.12	1.40	1.68	0.92	0.99	0.99
X-120×120×9.6-200×200×12×45°	0.47	1446.1	1619.1	0.98	1.27	1.53	0.87	0.99	0.94	1.10	1.42	1.71	0.93	1.01	1.00
X-120×120×12-200×200×12×45°	0.47	1501.0	1717.4	0.98	1.32	1.58	0.90	1.03	0.97	1.12	1.51	1.81	0.97	1.07	1.06
X-160×160×6-200×200×12×45°	0.62	1819.0	1985.8	1.27	0.88	1.46	0.91	0.98	0.96	1.39	0.96	1.59	0.95	1.12	1.00
X-160×160×7.8-200×200×12×45°	0.62	1882.7	2078.9	1.26	0.91	1.51	0.94	1.01	1.00	1.39	1.01	1.66	0.99	1.17	1.05
X-160×160×9.6-200×200×12×45°	0.62	1999.8	2290.9	1.29	0.97	1.60	0.99	1.08	1.06	1.48	1.11	1.83	1.08	1.29	1.15
X-160×160×12-200×200×12×45°	0.62	2122.2	2407.8	1.32	1.03	1.70	1.05	1.14	1.12	1.50	1.16	1.93	1.12	1.36	1.21
X-180×180×6-200×200×12×45°	0.70	2198.9	2365.5	1.60	0.86	1.52	1.01	0.92	1.04	1.73	0.92	1.63	1.04	1.31	1.06
X-180×180×7.8-200×200×12×45°	0.70	2300.0	2430.2	1.61	0.90	1.59	1.05	0.96	1.09	1.70	0.95	1.68	1.06	1.34	1.09
X-180×180×9.6-200×200×12×45°	0.70	2351.1	2485.8	1.59	0.92	1.62	1.07	0.98	1.12	1.68	0.97	1.72	1.07	1.37	1.12
X-180×180×12-200×200×12×45°	0.70	2437.0	2551.5	1.58	0.95	1.68	1.11	1.02	1.16	1.66	1.00	1.76	1.09	1.41	1.15
X-60×60×5-200×200×10×45°	0.23	695.6	826.3	0.90	1.46	1.54	0.98	0.99	0.90	1.07	1.73	1.83	1.03	0.96	0.97
X-60×60×6.5-200×200×10×45°	0.23	706.3	854.2	0.87	1.48	1.56	0.99	1.01	0.91	1.05	1.79	1.89	1.06	0.99	1.00
X-60×60×8-200×200×10×45°	0.23	748.5	910.0	0.89	1.57	1.65	1.05	1.07	0.97	1.09	1.91	2.01	1.12	1.06	1.07
X-60×60×10-200×200×10×45°	0.23	732.3	930.2	0.84	1.53	1.62	1.02	1.05	0.95	1.07	1.95	2.05	1.13	1.08	1.09
X-90×90×5-200×200×10×45°	0.34	789.9	956.3	0.85	1.33	1.45	0.90	0.95	0.89	1.03	1.61	1.75	0.97	0.94	0.97
X-90×90×6.5-200×200×10×45°	0.34	806.1	968.2	0.83	1.35	1.48	0.92	0.97	0.91	1.00	1.63	1.78	0.97	0.96	0.99
X-90×90×8-200×200×10×45°	0.34	820.4	994.8	0.82	1.38	1.50	0.93	0.99	0.92	0.99	1.67	1.82	0.99	0.98	1.01

X-90×90×10-200×200×10×45°	0.34	837.4	1005.5	0.80	1.41	1.54	0.95	1.01	0.94	0.96	1.69	1.84	0.99	0.99	1.03
X-120×120×5-200×200×10×45°	0.45	922.2	1088.0	0.89	1.17	1.40	0.88	0.94	0.90	1.05	1.38	1.65	0.92	0.94	0.96
X-120×120×6.5-200×200×10×45°	0.45	934.9	1123.3	0.86	1.18	1.42	0.89	0.95	0.92	1.04	1.42	1.70	0.95	0.97	0.99
X-120×120×8-200×200×10×45°	0.45	963.8	1154.6	0.86	1.22	1.46	0.92	0.98	0.94	1.03	1.46	1.75	0.96	0.99	1.02
X-120×120×10-200×200×10×45°	0.45	993.1	1187.6	0.85	1.26	1.51	0.94	1.01	0.97	1.02	1.50	1.80	0.98	1.02	1.05
X-160×160×5-200×200×10×45°	0.60	1225.1	1429.5	1.13	0.85	1.42	0.96	0.94	0.99	1.32	1.00	1.66	1.00	1.05	1.03
X-160×160×6.5-200×200×10×45°	0.60	1278.1	1495.5	1.13	0.89	1.49	1.00	0.98	1.03	1.32	1.04	1.74	1.04	1.10	1.08
X-160×160×8-200×200×10×45°	0.60	1321.1	1548.5	1.12	0.92	1.54	1.04	1.02	1.07	1.32	1.08	1.80	1.06	1.14	1.12
X-160×160×10-200×200×10×45°	0.60	1312.3	1565.1	1.08	0.91	1.53	1.03	1.01	1.06	1.28	1.09	1.82	1.06	1.15	1.13
X-180×180×5-200×200×10×45°	0.68	1510.8	1717.0	1.45	0.88	1.53	1.09	0.86	1.10	1.65	1.00	1.73	1.10	1.10	1.11
X-180×180×6.5-200×200×10×45°	0.68	1550.3	1780.9	1.42	0.91	1.57	1.12	0.88	1.13	1.63	1.04	1.80	1.13	1.14	1.16
X-180×180×8-200×200×10×45°	0.68	1671.5	1936.7	1.48	0.98	1.69	1.20	0.95	1.22	1.72	1.13	1.96	1.22	1.24	1.26
X-180×180×10-200×200×10×45°	0.68	1736.8	2122.0	1.48	1.02	1.75	1.25	0.98	1.27	1.81	1.24	2.14	1.32	1.36	1.38
X-60×60×4-200×200×8×45°	0.22	422.0	530.1	0.76	1.38	1.42	1.03	1.03	0.91	0.96	1.73	1.78	1.03	0.95	0.94
X-60×60×5.2-200×200×8×45°	0.22	423.2	564.2	0.73	1.38	1.42	1.03	1.03	0.91	0.97	1.85	1.89	1.08	1.01	1.00
X-60×60×6.4-200×200×8×45°	0.22	422.6	564.7	0.70	1.38	1.42	1.02	1.03	0.91	0.94	1.85	1.89	1.08	1.01	1.00
X-60×60×8-200×200×8×45°	0.22	449.8	611.3	0.72	1.47	1.51	1.09	1.10	0.97	0.98	2.00	2.05	1.15	1.10	1.08
X-90×90×4-200×200×8×45°	0.33	463.9	603.0	0.70	1.22	1.29	0.91	0.95	0.87	0.91	1.58	1.68	0.95	0.91	0.93
X-90×90×5.2-200×200×8×45°	0.33	468.9	618.1	0.67	1.23	1.31	0.92	0.96	0.88	0.89	1.62	1.72	0.96	0.94	0.95
X-90×90×6.4-200×200×8×45°	0.33	478.1	627.3	0.66	1.25	1.33	0.94	0.98	0.90	0.87	1.65	1.75	0.97	0.95	0.97
X-90×90×8-200×200×8×45°	0.33	487.3	643.0	0.65	1.28	1.36	0.95	1.00	0.92	0.86	1.69	1.79	0.98	0.97	0.99
X-120×120×4-200×200×8×45°	0.45	543.3	697.6	0.73	1.07	1.26	0.90	0.94	0.89	0.94	1.38	1.61	0.92	0.92	0.93
X-120×120×5.2-200×200×8×45°	0.45	558.0	717.2	0.72	1.10	1.29	0.92	0.96	0.92	0.93	1.42	1.66	0.94	0.94	0.96
X-120×120×6.4-200×200×8×45°	0.45	547.5	726.1	0.68	1.08	1.27	0.90	0.94	0.90	0.91	1.44	1.68	0.94	0.95	0.97
X-120×120×8-200×200×8×45°	0.45	579.3	746.6	0.70	1.15	1.34	0.95	1.00	0.95	0.90	1.48	1.73	0.96	0.98	1.00
X-160×160×4-200×200×8×45°	0.59	732.7	921.5	0.94	0.80	1.31	1.00	0.94	0.99	1.18	1.00	1.64	1.00	1.01	1.01
X-160×160×5.2-200×200×8×45°	0.59	757.0	961.5	0.93	0.82	1.35	1.03	0.97	1.03	1.18	1.05	1.71	1.04	1.05	1.05
X-160×160×6.4-200×200×8×45°	0.59	777.5	993.1	0.92	0.85	1.38	1.06	1.00	1.05	1.18	1.08	1.77	1.06	1.09	1.09
X-160×160×8-200×200×8×45°	0.59	811.4	1038.9	0.93	0.88	1.45	1.10	1.04	1.10	1.19	1.13	1.85	1.10	1.14	1.14
X-180×180×4-200×200×8×45°	0.67	911.4	1157.8	1.22	0.88	1.41	1.14	0.85	1.12	1.55	1.11	1.80	1.16	1.07	1.14
X-180×180×5.2-200×200×8×45°	0.67	935.1	1179.0	1.20	0.90	1.45	1.17	0.87	1.15	1.51	1.13	1.83	1.17	1.09	1.16
X-180×180×6.4-200×200×8×45°	0.67	983.0	1255.6	1.22	0.95	1.52	1.23	0.91	1.20	1.56	1.21	1.95	1.23	1.16	1.24
X-180×180×8-200×200×8×45°	0.67	1000.1	1350.2	1.19	0.96	1.55	1.25	0.93	1.23	1.61	1.30	2.09	1.31	1.25	1.33
X-60×60×3.33-200×200×6.66×45°	0.22	256.5	373.7	0.61	1.21	1.21	0.99	0.99	0.86	0.89	1.76	1.76	1.03	0.95	0.93
X-60×60×4.33-200×200×6.66×45°	0.22	265.3	403.2	0.60	1.25	1.25	1.02	1.02	0.89	0.91	1.90	1.90	1.10	1.03	1.00
X-60×60×5.33-200×200×6.66×45°	0.22	263.0	390.6	0.58	1.24	1.24	1.01	1.01	0.88	0.86	1.84	1.84	1.06	0.99	0.97
X-60×60×6.66-200×200×6.66×45°	0.22	276.8	414.7	0.58	1.30	1.30	1.06	1.07	0.93	0.88	1.95	1.95	1.11	1.06	1.03

X-90×90×3.33-200×200×6.66×45°	0.33	287.6	413.7	0.57	1.09	1.13	0.89	0.93	0.85	0.82	1.56	1.62	0.93	0.89	0.89
X-90×90×4.33-200×200×6.66×45°	0.33	293.5	418.7	0.55	1.11	1.15	0.91	0.95	0.86	0.79	1.58	1.64	0.93	0.90	0.90
X-90×90×5.33-200×200×6.66×45°	0.33	299.6	428.6	0.55	1.13	1.18	0.93	0.97	0.88	0.78	1.62	1.68	0.94	0.92	0.92
X-90×90×6.66-200×200×6.66×45°	0.33	308.4	451.7	0.54	1.16	1.21	0.95	1.00	0.91	0.79	1.71	1.77	0.98	0.97	0.97
X-120×120×3.33-200×200×6.66×45°	0.44	341.7	483.4	0.61	0.97	1.11	0.89	0.93	0.88	0.86	1.38	1.58	0.91	0.90	0.91
X-120×120×4.33-200×200×6.66×45°	0.44	351.0	495.2	0.60	1.00	1.14	0.92	0.95	0.90	0.84	1.41	1.61	0.92	0.92	0.93
X-120×120×5.33-200×200×6.66×45°	0.44	359.4	504.5	0.59	1.02	1.17	0.94	0.98	0.92	0.83	1.44	1.65	0.93	0.94	0.94
X-120×120×6.66-200×200×6.66×45°	0.44	365.2	523.7	0.58	1.04	1.19	0.95	0.99	0.94	0.83	1.49	1.71	0.96	0.97	0.98
X-160×160×3.33-200×200×6.66×45°	0.59	468.3	649.1	0.79	0.73	1.18	1.01	0.94	0.99	1.10	1.02	1.63	1.01	0.99	1.00
X-160×160×4.33-200×200×6.66×45°	0.59	488.5	677.4	0.79	0.77	1.23	1.05	0.98	1.04	1.10	1.06	1.71	1.04	1.03	1.04
X-160×160×5.33-200×200×6.66×45°	0.59	504.2	699.6	0.79	0.79	1.27	1.08	1.01	1.07	1.09	1.10	1.76	1.07	1.07	1.08
X-160×160×6.66-200×200×6.66×45°	0.59	500.7	725.0	0.75	0.78	1.26	1.07	1.00	1.06	1.09	1.14	1.83	1.09	1.10	1.12
X-180×180×3.33-200×200×6.66×45°	0.66	570.0	770.0	1.00	0.82	1.25	1.13	0.82	1.10	1.36	1.11	1.69	1.10	0.97	1.07
X-180×180×4.33-200×200×6.66×45°	0.66	606.7	832.0	1.02	0.87	1.33	1.20	0.87	1.17	1.40	1.20	1.83	1.18	1.05	1.15
X-180×180×5.33-200×200×6.66×45°	0.66	629.8	861.8	1.03	0.91	1.38	1.24	0.90	1.21	1.40	1.24	1.89	1.21	1.09	1.20
X-180×180×6.66-200×200×6.66×45°	0.66	612.0	860.0	0.96	0.88	1.34	1.20	0.88	1.18	1.35	1.24	1.89	1.19	1.08	1.19
X-60×60×2.5-200×200×5×45°	0.22	115.4	200.8	0.42	0.97	0.93	0.92	0.99	0.85	0.73	1.68	1.62	0.96	0.88	0.84
X-60×60×3.25-200×200×5×45°	0.22	115.7	202.5	0.40	0.97	0.93	0.92	0.99	0.85	0.71	1.70	1.63	0.96	0.89	0.85
X-60×60×4-200×200×5×45°	0.22	121.9	220.2	0.41	1.02	0.98	0.97	1.04	0.90	0.74	1.84	1.77	1.04	0.97	0.92
X-60×60×5-200×200×5×45°	0.22	121.0	225.0	0.39	1.01	0.97	0.96	1.04	0.89	0.73	1.88	1.81	1.05	0.99	0.94
X-90×90×2.5-200×200×5×45°	0.33	130.7	221.8	0.40	0.88	0.88	0.85	0.94	0.84	0.67	1.49	1.49	0.86	0.82	0.81
X-90×90×3.25-200×200×5×45°	0.33	132.0	224.3	0.38	0.89	0.89	0.85	0.95	0.85	0.65	1.51	1.51	0.86	0.83	0.82
X-90×90×4-200×200×5×45°	0.33	136.3	218.0	0.38	0.92	0.92	0.88	0.98	0.88	0.61	1.46	1.47	0.83	0.81	0.80
X-90×90×5-200×200×5×45°	0.33	137.4	234.3	0.37	0.92	0.92	0.89	0.98	0.89	0.63	1.57	1.57	0.88	0.87	0.86
X-120×120×2.5-200×200×5×45°	0.44	160.1	267.7	0.44	0.81	0.90	0.87	0.96	0.90	0.73	1.36	1.50	0.87	0.85	0.85
X-120×120×3.25-200×200×5×45°	0.44	165.1	275.3	0.43	0.84	0.92	0.90	0.99	0.93	0.72	1.39	1.54	0.89	0.88	0.87
X-120×120×4-200×200×5×45°	0.44	159.2	267.0	0.40	0.81	0.89	0.87	0.96	0.90	0.67	1.35	1.49	0.86	0.85	0.85
X-120×120×5-200×200×5×45°	0.44	170.0	290.0	0.41	0.86	0.95	0.92	1.02	0.96	0.71	1.47	1.62	0.92	0.92	0.92
X-160×160×2.5-200×200×5×45°	0.58	228.1	360.1	0.59	0.64	0.99	1.03	1.00	1.07	0.94	1.00	1.56	0.97	0.93	0.94
X-160×160×3.25-200×200×5×45°	0.58	233.1	383.0	0.58	0.65	1.01	1.05	1.02	1.09	0.95	1.07	1.66	1.02	0.98	1.00
X-160×160×4-200×200×5×45°	0.58	241.1	400.2	0.58	0.67	1.04	1.08	1.06	1.13	0.96	1.12	1.73	1.06	1.03	1.05
X-160×160×5-200×200×5×45°	0.58	248.4	415.0	0.58	0.69	1.08	1.11	1.09	1.16	0.96	1.16	1.80	1.08	1.07	1.09
X-180×180×2.5-200×200×5×45°	0.66	290.1	489.0	0.79	0.78	1.10	1.20	0.90	1.23	1.33	1.32	1.85	1.21	1.02	1.16
X-180×180×3.25-200×200×5×45°	0.66	293.6	495.6	0.76	0.79	1.11	1.21	0.91	1.25	1.29	1.34	1.88	1.22	1.03	1.17
X-180×180×4-200×200×5×45°	0.66	309.8	500.0	0.78	0.84	1.17	1.28	0.96	1.32	1.25	1.35	1.89	1.22	1.04	1.18
X-180×180×5-200×200×5×45°	0.66	301.9	510.0	0.73	0.81	1.14	1.24	0.94	1.28	1.23	1.37	1.93	1.23	1.06	1.20
X-50×100×4-150×150×6×45°	0.25	241.2*	307.2*	0.60	1.16	1.38	1.00	0.88	0.91	0.77	1.48	1.76	1.00	0.82	0.94

X-100×50×4-150×150×6×45°	0.50	281.7*	350.1*	0.78	1.08	1.08	0.80	1.04	0.80	0.97	1.34	1.35	0.78	1.00	0.80
X-50×100×4-120×120×4×45°	0.31	109.2*	149.9*	0.47	1.13	1.38	1.11	0.97	1.05	0.64	1.55	1.90	1.05	0.87	1.03
X-100×50×4-120×120×4×45°	0.62	153.6*	-	0.88	0.88	1.14	1.01	1.28	0.99	-	-	-	-	-	-
X-50×100×4-120×120×3×45°	0.30	59.6*	88.7*	0.34	0.93	1.12	1.05	0.95	1.04	0.51	1.38	1.66	0.92	0.75	0.90
X-100×50×4-120×120×3×45°	0.61	92.0*	-	0.71	0.76	1.00	1.02	1.24	1.05	-	-	-	-	-	-
X-80×80×4-140×140×4×45°	0.42	106.5*	-	0.45	0.82	1.02	0.90	0.98	0.90	-	-	-	-	-	-
X-80×80×4-120×120×4×45°	0.50	139.7*	180.8*	0.61	1.24	1.30	1.07	1.15	1.07	0.79	1.60	1.68	0.96	1.02	0.98
X-80×80×4-120×120×3×45°	0.48	75.4*	-	0.45	0.86	1.04	0.99	1.07	1.03	-	-	-	-	-	-
X-80×80×4-120×120×3×45°-R	0.48	76.6*	-	0.45	0.89	1.06	1.02	1.10	1.06	-	-	-	-	-	-
Mean (P_m)				0.82	1.06	1.32	1.00	0.99	0.99	1.08	1.42	1.75	1.02	1.02	1.02
COV (V_p)				0.375	0.226	0.174	0.109	0.069	0.118	0.273	0.201	0.078	0.102	0.124	0.109
Resistance factor (ϕ)				1.00	1.00	1.00	0.80	0.85	0.80	1.00	1.00	1.00	0.85	0.80	0.85
Reliability index (β_0)				0.70	1.56	2.45	2.67	2.52	2.60	1.57	2.53	3.91	2.56	2.67	2.52

Note: " - " denotes not applicable; " * " data obtained from Pandey and Young [2].

Table 7. Values of coefficients for SBB T- and X-joints unified design equation.

Joint Types	Joint Resistance	Coefficients					
		A	B	C	D	E	F
SBB T-joint	Joint failure strength	1.5	0.6	1	9	1.2	-0.002
	Ultimate capacity	1.7	0.7	1	7	1.1	-0.01
SBB X-joint	Joint failure strength	2	0.5	0.1	7	0.6	0.02
	Ultimate capacity	2	0.5	0.5	8	1.1	-0.003